Journal of
Composites Science

MDPI

Article

Numerical Modeling of Single-Lap Shear Bond Tests for Composite-Reinforced Mortar Systems

Rossana Dimitri *, Martina Rinaldi, Marco Trullo and Francesco Tornabene

Department of Innovation Engineering, School of Engineering, University of Salento, 73100 Lecce, Italy; francesco.tornabene@unisalento.it (F.T.)
* Correspondence: rossana.dimitri@unisalento.it

Abstract: The large demand of reinforcement systems for the rehabilitation of existing concrete and masonry structures, has recently increased the development of innovative methods and advanced systems where the structural mass and weight are reduced, possibly avoiding steel reinforcements, while using non-invasive and reversible reinforcements made of pre-impregnated fiber nets and mortars in the absence of cement, commonly known as composite-reinforced mortars (CRMs). To date, for such composite materials, few experimental studies have been performed. Their characterization typically follows the guidelines published by the Supreme Council of Public Works. In such a context, the present work aims at studying numerically the fracturing behavior of CRM single-lap shear tests by implementing a cohesive zone model and concrete damage plasticity, in a finite element setting. These specimens are characterized by the presence of a mortar whose mechanical behavior has been defined by means of an analytical approximation based on exponential or polynomial functions. Different fracturing modes are studied numerically within the CRM specimen, involving the matrix and reinforcement phases, as well as the substrate-to-CRM interface. Based on a systematic investigation, the proposed numerical modeling is verified to be a useful tool to predict the response of the entire reinforcement system, in lieu of more costly experimental tests, whose results could be useful for design purposes and could serve as reference numerical solutions for further analytical/experimental investigations on the topic.

Keywords: concrete; CRM; debonding; fiber/matrix bond; finite element analysis (FEA); interfaces

Citation: Dimitri, R.; Rinaldi, M.; Trullo, M.; Tornabene, F. Numerical Modeling of Single-Lap Shear Bond Tests for Composite-Reinforced Mortar Systems. *J. Compos. Sci.* **2023**, 7, 329. https://doi.org/10.3390/jcs7080329

Academic Editor: Zhong Hu

Received: 2 July 2023
Revised: 5 August 2023
Accepted: 8 August 2023
Published: 14 August 2023

1. Introduction

In recent decades, an increased use of alternative techniques instead of traditional retrofitting systems, such as the innovative materials involved in externally bonded reinforcements (EBRs), has been noticed among the scientific community. Composite strengthening solutions adopting fiber-reinforced polymers (FRPs) have been commonly used for the reinforcement of masonry [1–4] and concrete [5–7] substrates. However, despite the use of polymer (organic) adhesives, FRP composites are both incompatible with masonry substrates and hard to remove [8,9]. Furthermore, concrete substrates are typically characterized by a low tensile strength, so that strengthening effects cannot be fully employed due to a premature debonding failure of the FRP reinforcement [10,11]. As a result, an extensive research has been performed in the literature on the bond behavior of FRP-to-concrete joints, leading scientists to propose a large amount of bond strength and bond-slip models [12–19].

To overcome such FRP drawbacks, inorganic binders are increasingly used in the matrix, in the form of open-mesh textiles instead of continuous fiber sheets, as commonly occurs in the so-called composite-reinforced mortar (CRM) [20–29]. The application of CRM guarantees a better compatibility with masonry substrates due to the high vapor permeability of mortar. Moreover, this system is sustainable and reversible, it can be easily applied also on irregular substrates, on wet support, and it features better performance at elevated temperatures.

Differently from FRP, in which chemical bonds derived from a polymerization process of the organic matrix at the interfacial level between the fiber and resin, the interaction between the mortar matrix and fibers in CRMs is typically mechanical. It depends on many factors, e.g., the mortar penetration in the mesh space and the friction at the matrix–fiber interface during the slip stage. It is well known from the literature that CRM is made by a rigid grid of pre-cured FRP. More specifically, composite yarns and pultruded elements characterize the warp and the weft direction, respectively, where the composite yarns are twisted both together and around the pultruded elements, making possible the realization of a stable bi-directional grid and replacing the steel grid used in the ferrocement traditional technique [30,31]. Considering the entire CRM system, the mortar is a key member that withstands the load-carrying capacity, being fundamental for transferring the stress between the externally bonded reinforcement and the substrate. Thus, the overall behavior of the CRM, along with its interaction with substrates, and the possible effect of anchors should be considered for a complete characterization of the system.

In such a context, however, the scientific literature focusing on CRM systems seems to be quite limited, mainly because of the difficulty in defining some reliable design procedures [27]. At the same time, there are no works in which CRMs are analyzed computationally by three-dimensional models of single-lap shear bond tests. These tests are commonly used to characterize the shear behavior of composite-to-substrate joints, which dictates the sensitivity of the local and global response of the reinforcement phase and of the overall reinforced structure. On the contrary, a large variety of works can be found in the literature on the numerical study of fiber-reinforced cementitious mortar (FRCM) specimens, which are similar to CRM but with a soft and dry textile sheet [32–37].

According to the national guidelines, the single-lap shear bond tests conducted on FRCMs can have as a final result different failure modes [38] depending on the matrix thickness, the mechanical characteristics of the composite and substrate, and the substrate treatment: (a) debonding of the fiber at the matrix–fiber interface; (b) interlaminar failure of the matrix; (c) detachment of the entire composite strip without damage to the substrate; (d) debonding of the composite strip within the substrate; (e) debonding of the fiber at the matrix–fiber interface followed by spalling of the matrix that covers the textile; and (f) rupture of the fibers.

Based on the lacking literature, the present work aims at modeling numerically a single-lap shear bond test by validating the model against existing predictions from the literature. To this end, we apply a cohesive zone model (CZM), as implemented in a classical finite element code, in order to investigate the crack initiation and propagation processes within materials and at interfaces with a good accuracy. A nonlinear traction–separation law describes the cohesive behavior at the interfacial level, with an ascending branch up to the peak load, followed by a softening branch, at which the fracturing process takes place [39]. The CZM was proposed for the first time by Barenblatt [40,41] and Dugdale [42] for the study of singularity-driven fracture mechanics, and it was then extended in the literature to study the fracturing process in many bi-material members [43–55], involving different loading conditions [56–61], scales [62–66], and FRP composite films [67–73].

Another analytical tool is proposed here to simulate the damage process of our specimens, namely, a concrete damage plasticity (CDP) model, which is considered as one of the most reliable models in the literature for studying the nonlinear fracturing of most materials. Starting from this model, and using different computational approaches, different damage models have been increasingly developed in the literature with the aim of developing novel stress–strain relationships both in compression and tension, or to propose innovative functions for the definition of damage parameters in compression (d_c) and tension (d_t). In the study of Lubliner et al. [67], a novel constitutive plastic model was proposed for the nonlinear analysis of concrete materials, involving different elastic and plastic stiffness degradation effects, in order to define a new yield criterion. The model was then validated by means a double numerical and experimental check of results with accurate predictions. Carol et al. [68] proposed some closed-form solutions for a correct definition of the tensile

damage for different loading cases. At the same time, Ahmed et al. [74] introduced a novel three-dimensional stress–strain relation based on the definition of a novel stress accounting for the shear damage. This stress state decomposes tensile and compressive parts into pure biaxial shear and pure tensile/compressive biaxial stresses. Through the theory of Lubliner et al. [67], a modified version of the damage concrete model was proposed by Lee et al. [75] for confinement purposes under uniform and non-uniform conditions. A model that overcomes any possible limitation of pure elastic–plastic damages during unloading phases was found by Jason et al. [76], while Grassl et al. [77] used the combination of damage mechanics and plasticity flow to investigate concrete structures subjected to dynamic loading conditions.

Based on the experimental results from the existing literature referring to single-lap shear tests [35], the present study aims at analyzing different possibilities of crisis mode for CRM reinforcements by evaluating comparatively the results in a systematic way in order to determine the governing damage mode. A novel analytical model is, thus, presented, that allows the mechanical response of the mortar to be described, and the fracturing behavior at the fiber–matrix and matrix–substrate interfaces, while using a classical CZM and CDP formulation. The results obtained from the numerical investigation can provide some useful insights for the design purposes of CRM systems and their associated engineering applications, starting from a full mechanical characterization of such strengthening materials and allowing their global response to be predicted for any type of material used.

After this introduction, in Section 2, we provide the main theoretical basics of the models here proposed as valid tools to study the fracturing problem of CRM systems, with their properties described in Section 3. The numerical investigation is discussed comparatively in Section 4, accounting for different geometrical schemes and fracturing mechanisms. The main findings can be found in the concluding Section 5, with valid suggestions both from an analytical and design standpoint.

2. Theoretical Formulation

2.1. Concrete Damage Plasticity Model

In this section, we briefly recall the main theoretical basics of the models applied herein for the study of the fracturing process in CRM single-lap shear bond tests. Due to the nonlinear and complex behavior of the mortar phase within specimens, a concrete damage plasticity (CDP) model is adopted, in a classical finite element environment, as proposed in the literature by Lee and Fenves [78] for concrete materials. This model requires the introduction of a yield function, as visible in Figure 1, where $\overline{q}$ is the Von Mises equivalent stress, defined as $\overline{q} = \sqrt{3(\mathbf{S} : \mathbf{S})/2}$, $\mathbf{S}$ is the deviatoric stress tensor, $\overline{p}$ is the hydrostatic pressure, $\widehat{\overline{\sigma}}_2$ is the maximum principal stress, and $\alpha \in (0.5; 1.0)$ is a function that depends on the biaxial compressive strength σ_{b0} and uniaxial compressive strength σ_{c0}. More specifically, α is defined as $\alpha = (\sigma_{b0}/\sigma_{c0} - 1)/(2\sigma_{b0}/\sigma_{c0} - 1)$, and β is the ratio of the second stress invariant on the tensile meridian, which affects the yield function shape in the deviatoric plane. At the same time, the uniaxial loading conditions in compression are described by three phases, as plotted in Figure 2, involving both the linear (step 1) and nonlinear (step 2) ascending branch together with the descending stage (step 3) of the constitutive relation.

In the first phase (phase 1 in Figure 2), the stress–strain relation has a linear behavior of the type

$$\sigma_c^1 = E_0 \varepsilon_c \tag{1}$$

At the end of this phase, the stress assumes a value of $\sigma_c = 0.4 f_{cm}$ according to EC2, where f_{cm} is the maximum compressive strength of the material and ε_c its relative compressive strain.

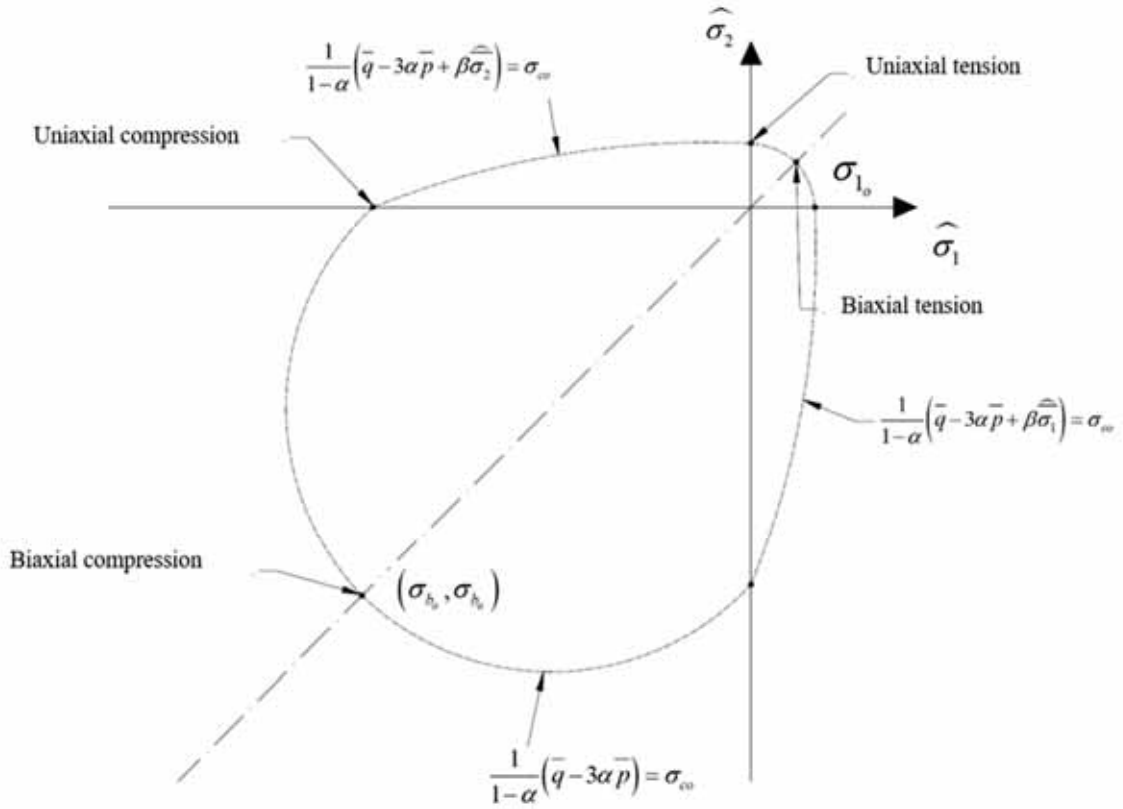

Figure 1. Concrete yield surface.

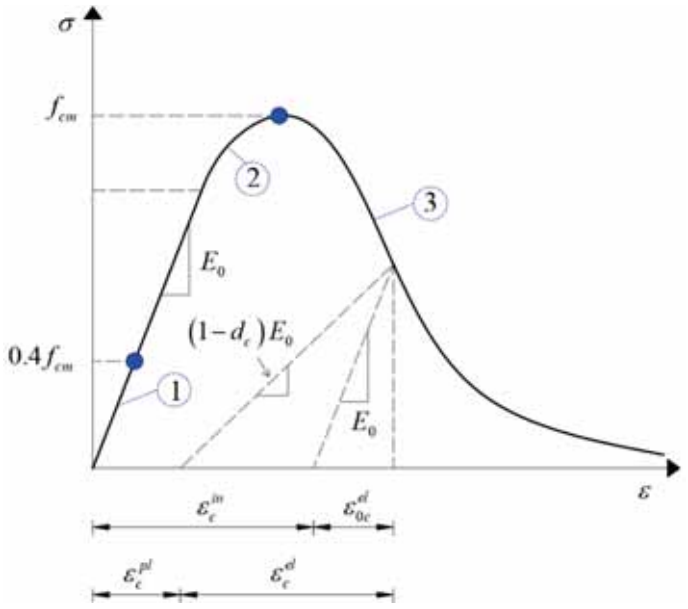

Figure 2. Constitutive relation in compression.

Once the compressive strength $\sigma_c = 0.4 f_{cm}$ is achieved, the material begins cracking, according to the following nonlinear behavior (phase 2 in Figure 2):

$$\sigma_c^2 = \frac{E_{ci}\frac{\varepsilon_c}{f_{cm}} - \left(\frac{\varepsilon_c}{\varepsilon_{c1}}\right)^2}{1 + \left(E_{ci}\frac{\varepsilon_{c1}}{f_{cm}} - 2\right)\frac{\varepsilon_c}{\varepsilon_{c1}}} f_{cm} \tag{2}$$

where E_{ci} is the modulus of elasticity of mortar and ε_{c1} is the deformation at σ_c^1.

The last phase (phase 3 in Figure 2) has a softening behavior and follows the theory proposed by Kratzig and Polling [79]:

$$\sigma_c^3 = \left(\frac{2 + \gamma_c f_{cm} \varepsilon_{c1}}{2 f_{cm}} - \gamma_c \varepsilon_c + \frac{\varepsilon_c^2 \gamma_c}{2 \varepsilon_{c1}} \right)^{-1} \tag{3}$$

with

$$\gamma_c = \frac{\pi^2 f_{cm} \varepsilon_{c1}}{2 \left[\frac{G_{ch}}{l_{eq}} - 0.5 f_{cm} \left(\varepsilon_{c1} (1 - b) + b \frac{f_{cm}}{E_0} \right) \right]^2} \tag{4}$$

where G_{ch} is the fracturing energy, $b = \varepsilon_c^{pl} / \varepsilon_c^{in}$ with ε_c^{pl} and ε_c^{in} are the plastic and inelastic strain, respectively, and l_{eq} is the length of the mesh element.

2.1.1. Behavior in Tension

A nonlinear tensile behavior is assumed for the mortar phase, as proposed by Hordijk [80], independently of the mesh size of the FEM-based elements, namely,

$$\frac{\sigma_t(w)}{f_{tm}} = \left[1 + \left(c_1 \frac{w}{w_c} \right)^3 \right] e^{-c_2 \frac{w}{w_c}} - \frac{w}{w_c} \left(1 + c_1^3 \right) e^{-c_2} \tag{5}$$

where $c_1 = 3$, $c_2 = 6.93$, and $w_c = 5.14 G_F / f_{tm}$ is the critical crack opening which depends on the fracture energy G_F and the maximum tensile strength of the material.

Based on the previous formulation, a novel curve can be obtained in the stress–displacement relation (Figure 3) through the following equation:

$$\varepsilon_t = \varepsilon_{tm} + \frac{w}{l_{eq}} \tag{6}$$

where ε_{tm} is the strain at the maximum tensile strength, ε_t is the strain at an arbitrary opening w, and l_{eq} is the length of the mesh element.

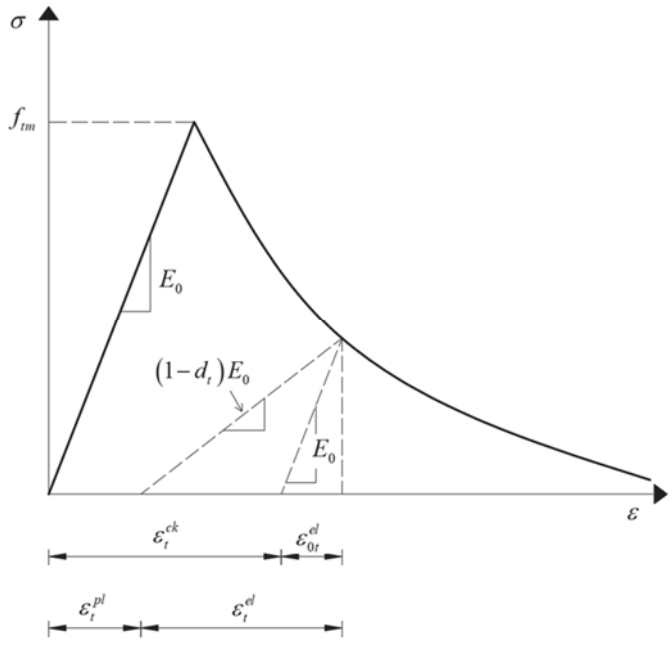

Figure 3. Behavior in tension.

2.1.2. Compressive Damage and Tension Damage Component

A compressive damage variable d_c is introduced to specify the compressive stiffness degradation damage, by means of the plastic strain ε_c^{pl} and constant factor b_c, with $0 \leq b_c \leq 1$

$$d_c = 1 - \frac{\sigma_c E_c^{-1}}{\varepsilon_c^{pl}(1/b_c - 1) + \sigma_c E_c^{-1}} \tag{7}$$

Similarly, a tension damage variable d_t is defined, which depends on the plastic strain ε_t^{pl} and the parameter b_t, namely,

$$d_t = 1 - \frac{\sigma_t E_t^{-1}}{\varepsilon_t^{pl}(1/b_t - 1) + \sigma_t E_t^{-1}} \tag{8}$$

2.2. Cohesive Zone Modeling

A further theoretical tool adopted here for our numerical investigation relies on the cohesive zone modeling, as proposed in the literature by Camanho et al. [62], to capture the mixed-mode delamination onset and growth in composite structural components. In such a context, a bi-linear behavior is proposed in line with Ref. [62] to define the process zone and cohesive zone for modes I, II, and III, by means of the mechanical parameters plotted in Figure 4.

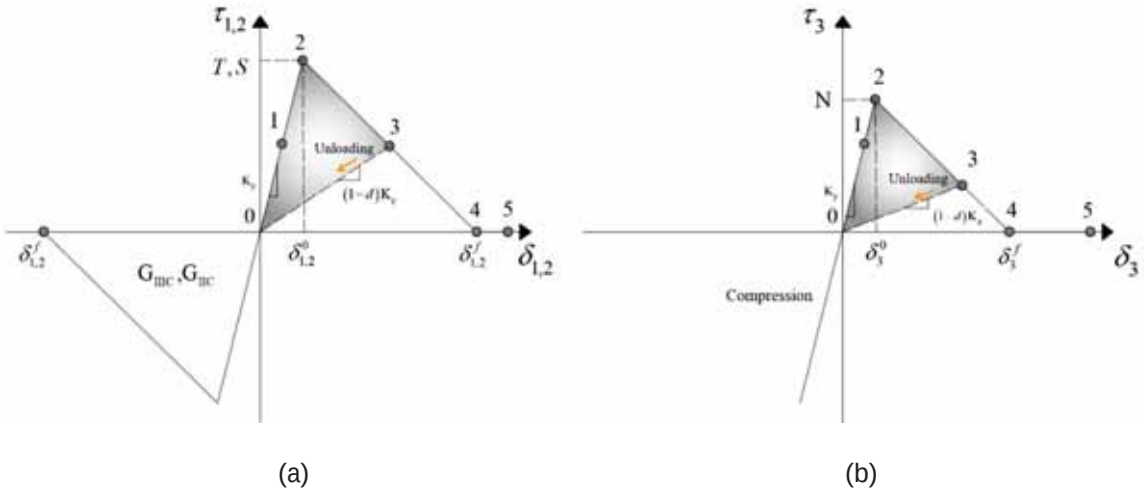

Figure 4. Pure mode constitutive laws: (**a**) mode II or mode III; (**b**) mode I.

As visible in this figure, each cohesive law requires a high initial stiffness, named as penalty stiffness, K, in the linear elastic range (point 1, Figure 4). Once the interlaminar tensile or shear strength is reached (point 2, Figure 4), the stiffness reduces gradually to zero. The onset displacements are obtained as: $\delta_3^0 = N/K$, $\delta_2^0 = S/K$, and $\delta_1^0 = T/K$, where N is the interlaminar tensile strength, whereas S and T are the interlaminar shear strengths. As known from the literature [81], cohesive zone models are related to the Griffith's fracture theory when the area under the traction–separation law corresponds to the fracture toughness (Figure 4), independently of the shape. As commented by Alfano and Crisfield [82], for the same displacement values δ_3^0 and δ_3^f (Figure 4), a perfect brittle failure is obtained, due to the sudden drop to zero of the load value. In this case, the model must be able to obtain the high stress gradients at the crack tip through a sufficiently fine mesh density or singular elements. Based on the definition of the area under the traction–separation laws (G_{IC}, G_{IIC}, G_{IIIC} for modes I, II, and III, respectively) it is possible to define the final displacements, δ_3^f, δ_2^f, δ_1^f, corresponding to the complete decohesion

$$\int_0^{\delta_3^f} \tau_3 d\delta_3 = G_{IC} \tag{9}$$

$$\int_0^{\delta_2^f} \tau_2 d\delta_2 = G_{IIC} \tag{10}$$

$$\int_0^{\delta_1^f} \tau_1 d\delta_1 = G_{IIIC} \tag{11}$$

such that the final displacements are defined as $\delta_3^f = 2G_{IC}/N$, $\delta_2^f = 2G_{IIC}/S$, and $\delta_1^f = 2G_{IIIC}/T$, respectively.

At points 4 and 5 in Figure 4, the crack is no longer capable of transferring loads and all the penalty stiffnesses go back to zero. At the same time, there is the necessity to avoid any interpenetration of the crack interfaces. This is possible by reintroducing the normal penalty stiffness when the interpenetration is detected. Camanho et al. [62] also defined the unloading behavior of a softening point up to the origin (Figure 4). By introducing the Macauley operator

$$\langle x \rangle = \begin{cases} 0, \text{ x } < 0 \\ x, \text{ x} \geq 0 \end{cases} \tag{12}$$

it is possible to describe the loading condition with the introduction of the maximum relative displacement, $\delta^{\max}$, defined as

$$\text{Mode II or III} : \delta_i^{\max} = \max\{\delta_i^{\max}, |\delta_i|\}, \ i = 1,2 \tag{13}$$

$$\text{Mode I} : \delta_i^{\max} = \max\{\delta_3^{\max}, \delta_3\}, \text{ with } \delta_3^{\max} \geq 0 \tag{14}$$

and by using a loading function, F, as follows

$$\text{Mode II or III} : F(|\delta_i| - \delta_i^{\max}) = \frac{\langle |\delta_i| - \delta_i^{\max} \rangle}{|\delta_i| - \delta_i^{\max}}, \ i = 1,2 \tag{15}$$

$$\text{Mode I} : F(\delta_3 - \delta_3^{\max}) = \frac{\langle \delta_3 - \delta_3^{\max} \rangle}{\delta_3 - \delta_3^{\max}}, \text{ with } \delta_3^{\max} \geq 0 \tag{16}$$

The parameter $\delta^{\max}$ is useful to consider the irreversibility of damage, as visible in Figure 4. Indeed, when the relative displacement is reduced, the curve decreases elastically to zero, with a reduced stiffness (point 3, in Figure 4).

The irreversible, bi-linear, softening constitutive behavior shown in Figure 4, referred to as single-mode loading, can be defined as follows [82–84]:

$$\tau_i = \begin{cases} K\delta_i, \ \delta_i^{\max} \leq \delta_i^0 \\ (1 - d_i)K\delta_i, \ \delta_i^0 < \delta_i^{\max} < \delta_i^f \\ 0, \ \delta_i^{\max} \geq \delta_i^f \end{cases} \tag{17}$$

$$d_i = \frac{\delta_i^f \left(\delta_i^{\max} - \delta_i^0\right)}{\delta_i^{\max}\left(\delta_i^f - \delta_i^0\right)}, \ i = 1,2,3; \ d_i \in [0,1] \tag{18}$$

The fundamental conditions to avoid interpenetration of the crack faces are as follows:

$$\tau_3 = K\delta_3, \ \delta_3 \leq 0 \tag{19}$$

which depends on the penalty stiffness, K, the corresponding fracture toughness, G_{IC}, G_{IIC} and G_{IIIC}, and the corresponding interlaminar tensile or shear strengths, N, S or T, respectively.

3. Bond Test and Materials

In their present state, the test methods applied to characterize CRM systems can be considered as an adjustment of existing methods commonly used for FRP and FRCM systems, for which many studies in the literature have already demonstrated the debonding performances as efficient reinforcement tools for different substrates [85–88]. It is well known from the literature that the debonding phenomenon is an undesirable brittle failure mode for structural safety, which is dictated by strength-reducing factors, thus making the quality and evaluation of the bond strength extremely important. In such a context, the present investigation aims at evaluating the debonding load of masonry or concrete elements strengthened with CRMs made of an inorganic matrix, instead of an organic resin as in FRP systems, and featuring different adhesion properties with substrates. The single-lap shear test, as here selected for our numerical investigation, is one of the most common experimental tests to evaluate the interfacial properties among strengthening systems and substrates [89,90], where a CRM reinforcement with length L, width B and thickness t is created directly on the substrate so that the mortar matures and chemically bonds to the surface, in line with Ref. [24]. One edge of the CRM net is pulled, while the substrate block is pushed by means of a reaction frame (i.e., compressed), as shown in Figure 5.

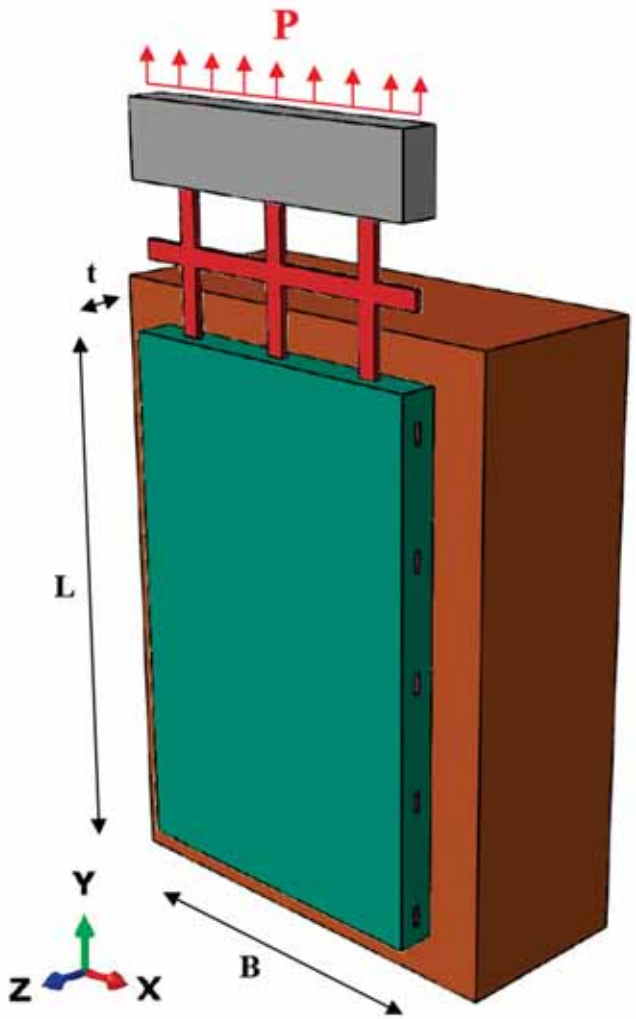

Figure 5. Single-lap direct shear test setup.

Three different sizes and boundary conditions have been accounted for herein to analyze the sensitivity of the fracture response, involving different possible crisis modes, i.e., the debonding of the fiber at the matrix–fiber interface, the detachment of the entire composite strip without damage of the substrate, and the interlaminar (delamination) failure of the matrix. More specifically, a CZM has been applied to model the fiber–matrix and matrix–substrate interfaces, whereas the CDP method has been applied to model the matrix. In this case, an analytical approximation has been implemented for a consistent modeling of the material behavior. Based on the experimental observations from Refs. [35,72,91–93], a smooth elastic-softening behavior of mortar specimens is expected for the load–displacement response, whose predictions can be approximated analytically by means of an exponential or a polynomial function, as proposed hereafter. We here consider both of them to investigate comparatively the effect of an asymptotic softening (exponential) function on the overall ductility response in lieu of a finite polynomial function, due to the different intrinsic mathematical nature.

Let start by considering an arbitrary exponential function of the type

$$f(x) = ax \cdot \mathrm{e}^{-bx} + c \tag{20}$$

where $f(x)$ represents the stress state $\sigma(\varepsilon)$, and x stands for the strain field ε, while a, b, and c are unknown parameters. By defining three boundary conditions, i.e., the null value of the function for $x = 0$, the initial stiffness value E_0, and the maximum stress value σ_{cu}, one obtains

$$\sigma(\varepsilon) = E_0 \varepsilon \mathrm{e}^{-[E_0/(\sigma_{cu}\mathrm{e})]\varepsilon} \tag{21}$$

Based on this equation, it is possible to describe the behavior of the mortar by defining the stiffness value $E_0 = 13$ GPa in the elastic phase, as well as the compression strength $\sigma_{cu} = 10.3$ MPa and tension strength $\sigma_{tu} = 2.2$ MPa of the inorganic matrix. This definition makes it possible to compare the mechanical behavior of the mortar described in Ref. [35] with that defined by Equation (21), as shown in Figure 6.

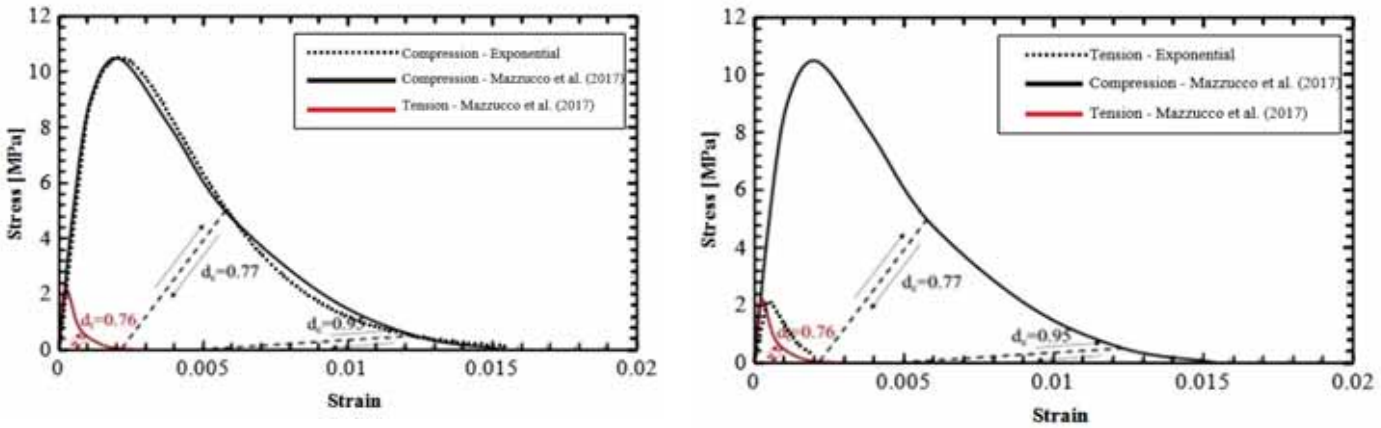

Figure 6. Constitutive relations in compression (**a**) and tension (**b**) as predicted in Ref. [35] and by our exponential approximation.

Another possible function has been chosen to approximate the mechanical response of the mortar, with an enhanced brittle behavior. In such a case, a less pronounced softening phase, with a steeper descending branch after the peak load, can be obtained by adopting a fourth-order polynomial of the type

$$f(x) = ax(x-b)(x-b)(x-2b) \tag{22}$$

whose lowest solution of its first derivative corresponds to the deformation ε_{c0}, i.e., the abscissa of the peak load σ_{c0}. Through these two boundary conditions it is possible to define the parameters a and b, such that the polynomial approximation becomes

$$f(x) = \frac{\sigma_{c0}}{33.97\varepsilon_{c0}^4} x\left(x - \frac{2\varepsilon_{c0}}{2-\sqrt{2}}\right)^2\left(x - \frac{4\varepsilon_{c0}}{2-\sqrt{2}}\right) \tag{23}$$

As visible in Figure 7, this definition also makes it possible to compare the mechanical behavior of the mortar for both loading–unloading states described by Ref. [35] and the polynomial Equation (23), both in compression (Figure 7a) and tension (Figure 7b).

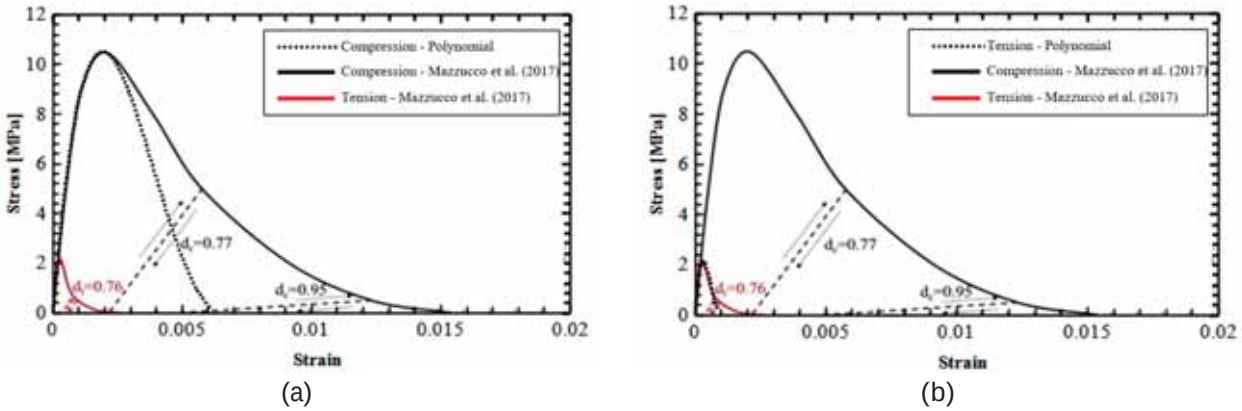

Figure 7. Constitutive relations in compression (**a**) and tension (**b**) as predicted in Mazzucco et al. [35] and by our polynomial approximation.

A comparative evaluation of the constitutive relations in compression and tension is also provided in Figure 8 for an inorganic mortar, where both approximations ensure the same compressive and tensile maximum stress value, while varying the ductility and initial stiffness of the material, especially in the tensile state. As expected, indeed, the softening branch related to the exponential equation is asymptotic, while it assumes a finite value of the total strain in the case of the polynomial approximation, with a clear increase in the ductility within the material in the first approximation.

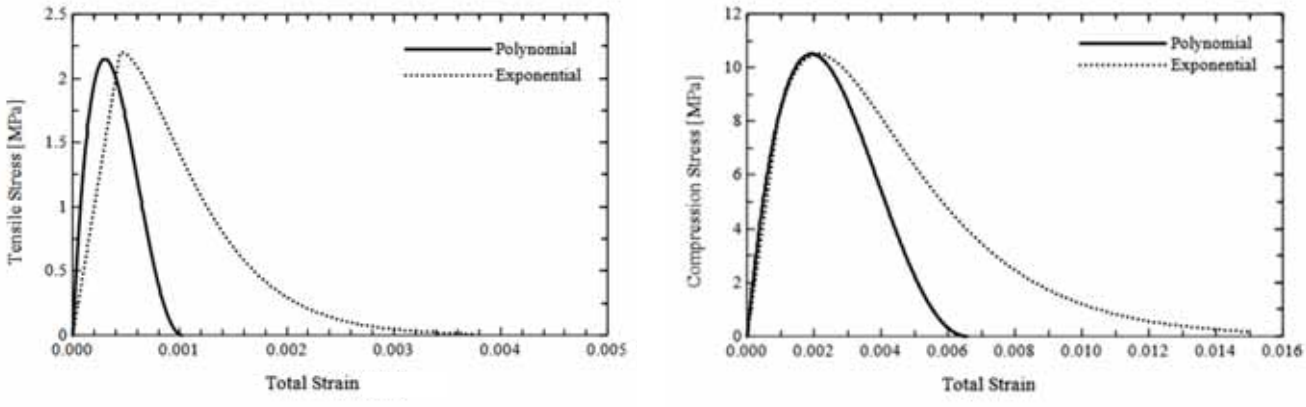

Figure 8. Analytical approximation from polynomial and exponential equations of a specimen in compression (**a**) and tension (**b**).

Two types of textile fiber reinforcement have been employed in the numerical model including wet or dry carbon fibers. Both types of fibers are characterized by three principal directions 1, 2, and 3 per bundle (Figure 9). The highest stiffness is reached in the direction of the fiber filaments (direction 1), while in the transversal directions 2 and 3,

the stiffness is defined by the coating matrix properties associated with a cable behavior. To reproduce this last behavior in the numerical code, an elastic orthotropic constitutive law has been considered, introducing nine constitutive parameters: three elastic moduli E_i, three Poisson's ratios $\nu_{i,j}$, and three shear moduli $G_{i,j}$—with $i, j = 1, 2, 3$ (see Figure 9). Both types of fiber net have been considered to assume a perfectly elastic behavior, according to the experimental predictions from the literature [35]. Moreover, the net is considered as a single solid to ensure the continuity at the corners between the longitudinal and transverse fibers (see Figure 9).

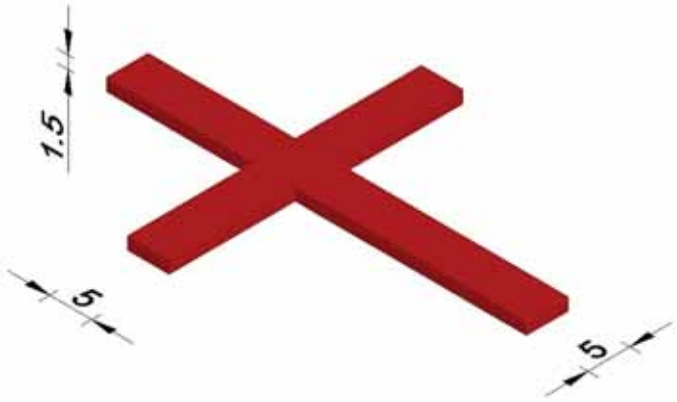

Figure 9. Detail of the fiber net in principal directions.

4. Numerical Investigation

The matrix stress–strain behavior is modeled by adopting the analytical approximations proposed in the previous section. More specifically, for the exponential approximation, the stiffness value is assumed to be equal to $E_0 = 13$ GPa in the elastic phase, while for the polynomial approximation the stiffness value is considered to be $E_0 = 8$ GPa. For both approximations, the compression and tensile strengths are assumed to be equal to $\sigma_{cu} = 10.5$ MPa and $\sigma_{tu} = 2.15$ MPa.

Two types of fibers were considered to define their mechanical properties. The first type accounts for transversal isotropic fibers, as considered by Mazzucco et al. [35], associated with dry carbon fibers, while the second type refers to pre-impregnated carbon fibers with an isotropic behavior, and a higher stiffness than the dry carbon fibers. Transversal isotropic fibers have an elastic modulus in the longitudinal and tangential directions equal to $E_1 = 68.10$ GPa and $E_2 = E_3 = 0.32$ GPa, respectively, while the Poisson's ratios are assumed to be $\nu_{1,2} = \nu_{2,3} = \nu_{1,3} = 0.35$.

The numerical study starts considering a reduced geometry for a small number of independent variables and a reduced computational time, whose geometry and dimensions are reported in Figure 10. Note that in this specimen there is only a single crossing of fibers, which makes it possible to validate the model while analyzing the mortar–net interaction in a critical point of the specimen. In line with the experimental predictions, for which the crisis does not affect the substrate, only the composite reinforcement was modeled and the matrix interface in contact with the masonry substrate was fully constrained. To reproduce the interlaminar (delamination) failure of the matrix, in this first example, the fiber–matrix interfaces were bundled with a tie constraint. This leads the damage to be concentrated only in the matrix, which can be studied separately from the behavior of the fiber–mortar interface. The mortar is here modeled with the CDP model and its mechanical properties derive from the analytical approximations in Equations (21) and (23). In Figure 11, the damage contour plot of the specimen is shown for both types of approximation and for wet fibers, with the same development of damage within the specimen for the polynomial (Figure 11a) and exponential (Figure 11b) approximations. A more extensive penetration of the matrix damage can be noticed in the specimen when dry carbon fibers are considered in the CRM specimen, as visible from the damage contour plots in Figure 12 (compared to

Figure 11), with a clear presence of stress concentrations at the transversal–longitudinal bundle joint corners. For each selected fiber, we have also evaluated the global load–slip response, as plotted in Figure 13, for both a polynomial and exponential approximation of the matrix mechanical properties, with a clear nonlinear behavior, where the matrix damage gradually increases after the onset of the nonlinear response, involving the matrix external side first, and then propagating along the fiber textile plane towards the loaded end secondly. In more detail, Figure 13a refers to wet fibers, while Figure 13b refers to dry carbon fibers, with a clear reduction in the peak load and initial stiffness in favor of a higher ductility of the material. Except for the initial linear elastic branch, the polynomial approximation of the matrix properties seems always to provide more conservative results compared to the exponential approximation in the nonlinear ascending and descending branches of the curves, due to the different intrinsic nature of both approximation functions. The numerical investigation considers also the effect of the cohesive fiber–matrix interface, as schematically shown in Figure 14, always for the reduced specimen reinforced with the stiffest fibers. The fiber–matrix interface is modeled accounting for the cohesive properties $f_1 = 0.24$ MPa, $f_2 = f_3 = 0.78$ MPa for the maximum nominal stresses in the three directions, and $\delta_1^f = 0.58$ mm, $\delta_2^f = 0.75$ mm, $\delta_3^f = 0.50$ mm, for the three ultimate values of displacement at the failure stage. Furthermore, the stiffness values in the three directions are assumed to be equal to $K_{nn} = K_{ss} = K_{tt} = 2215$ MPa.

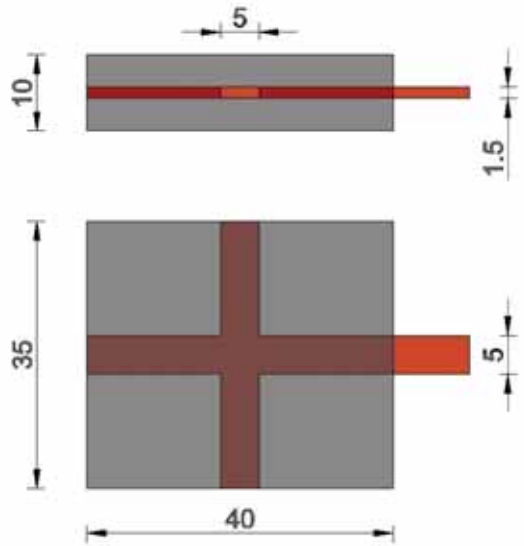

Figure 10. Reduced specimen. Geometric dimensions in mm.

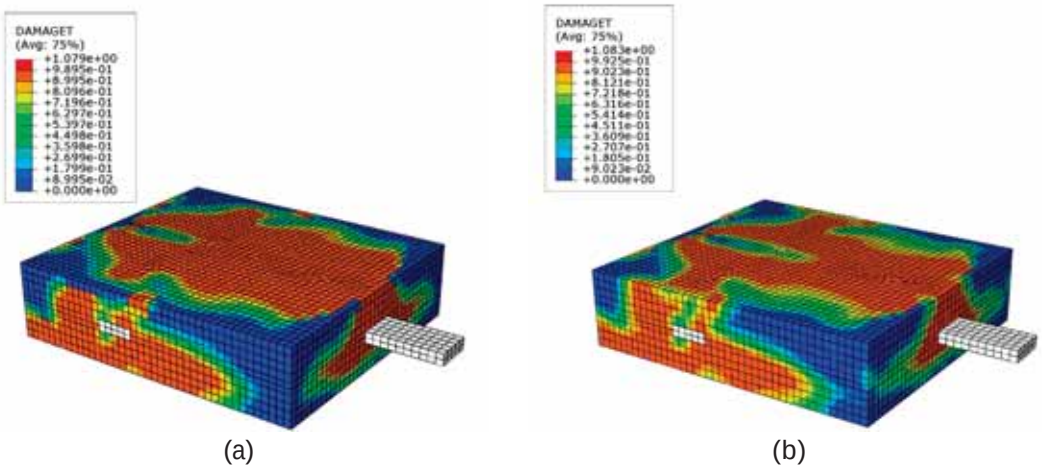

Figure 11. Matrix tensile damage contour for a polynomial (**a**) and exponential (**b**) approximation of a reduced specimen with wet fibers.

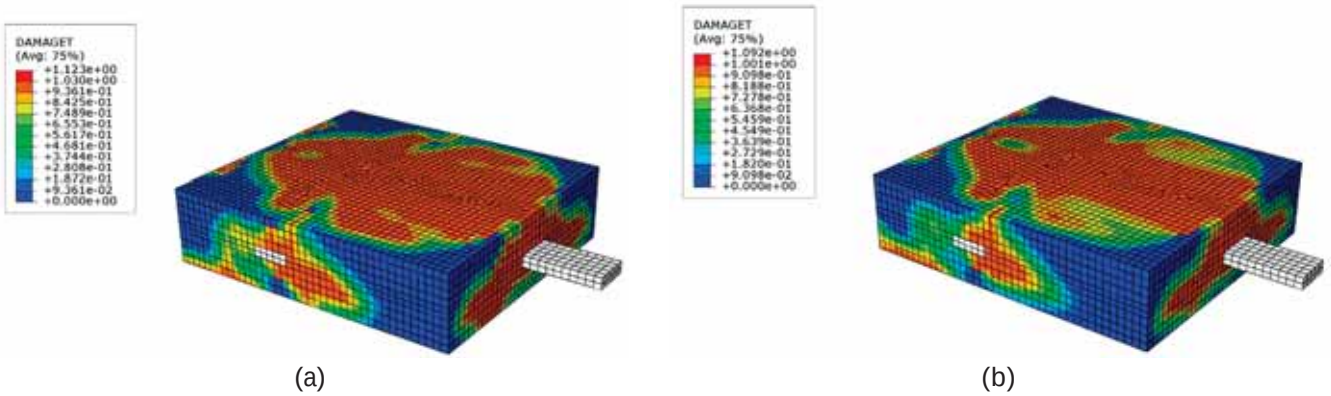

Figure 12. Matrix tensile damage contour for a polynomial (**a**) and exponential (**b**) approximation of a reduced specimen with dry fibers.

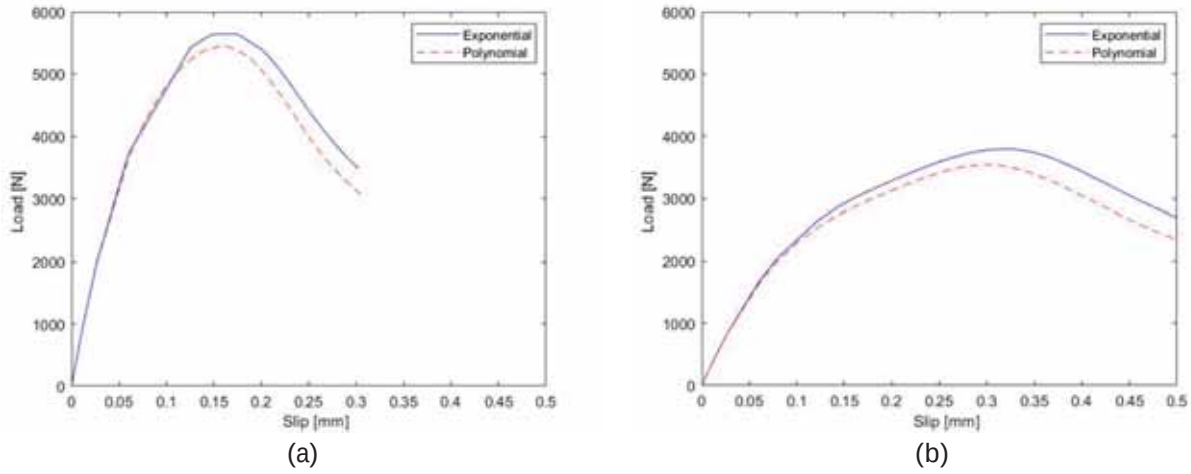

Figure 13. Comparison of the results for wet (**a**) and dry (**b**) carbon fibers.

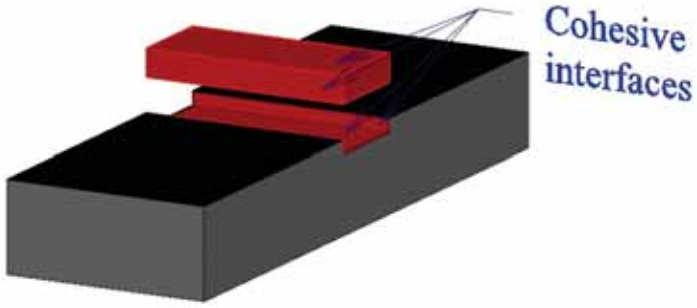

Figure 14. Detail of the fiber–matrix cohesive interfaces.

In Figure 15, we represent the damage contour plots of the reduced specimen in displacement control by applying a displacement of 0.35mm, always comparing the response provided by a polynomial (Figure 15a) and exponential (Figure 15b) approximation of the matrix properties, while reporting the global load–slip response in Figure 16. As visible from Figure 15, the transverse bundle tends to contrast the longitudinal slip pushing against the surrounding matrix, which starts becoming damaged at the transverse bundle–matrix interfaces, due to the presence of some stress concentration.

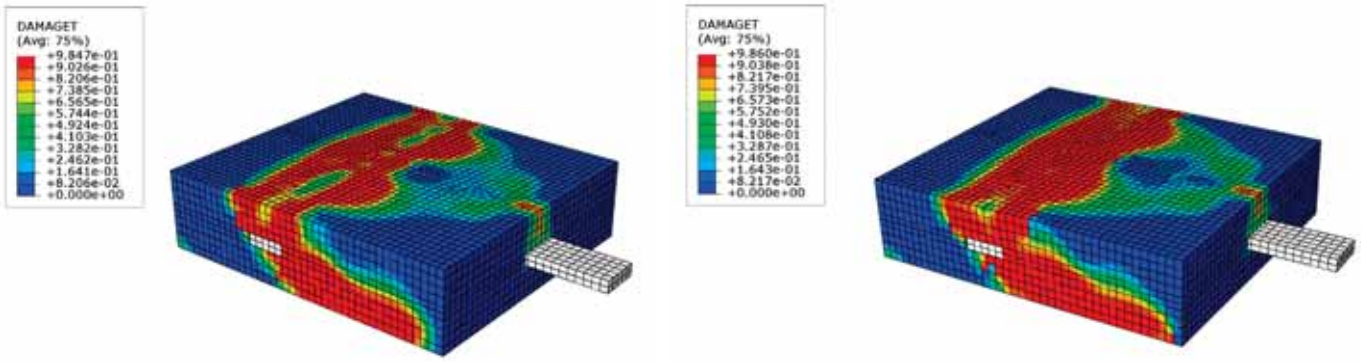

Figure 15. Matrix tensile damage contour for a polynomial (**a**) and exponential (**b**) approximation of a reduced specimen with a fiber–matrix cohesive interface and wet fibers.

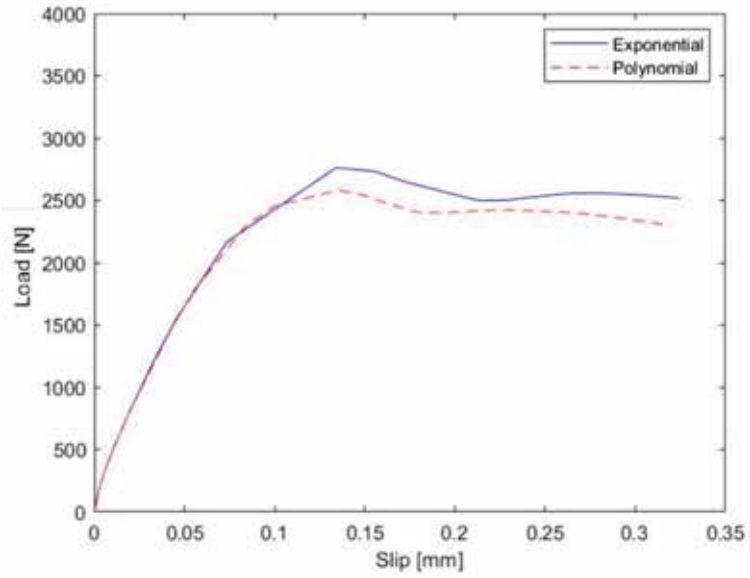

Figure 16. Load vs. slip response of the specimen modeled with a cohesive matrix–fiber interface.

The global response in Figure 16 seems to be slightly affected by the matrix properties, with an oscillating behavior after the peak load during the debonding stage between the matrix and fibers. Figure 16 clearly shows a first loss in resistance of the specimen, related to the first peak load, due to the decohesion among the fibers and the matrix. After that, the mortar resistance ensures a further increase in strength until the final collapse.

In the curves of Figures 13 and 16, it is possible to note that the overall response of the specimen modeled with an exponential approximation reaches slightly higher values of resistance due to the different maximum tensile strength, as visible in Figure 8. The same study was carried out for a larger specimen with the same mechanical properties. In this case, the reinforcement net has a higher number of transverse and longitudinal elements. In more detail, the net consists of two fibers in the longitudinal direction, and four fibers in the transverse direction. The dimensions are those shown in Figure 17.

In addition, in this case, the analysis starts considering a perfectly bonded fiber–matrix interface, where the specimen is loaded in the longitudinal direction at one side, while keeping fixed all the other sides. The contour plots of Figures 18 and 19 refer to a deformed configuration of the same specimen for wet (Figure 18) or dry (Figure 19) fiber reinforcements, with an extensive matrix cracking near the maximum peak value, which is, in turn, responsible for the decreased applied load.

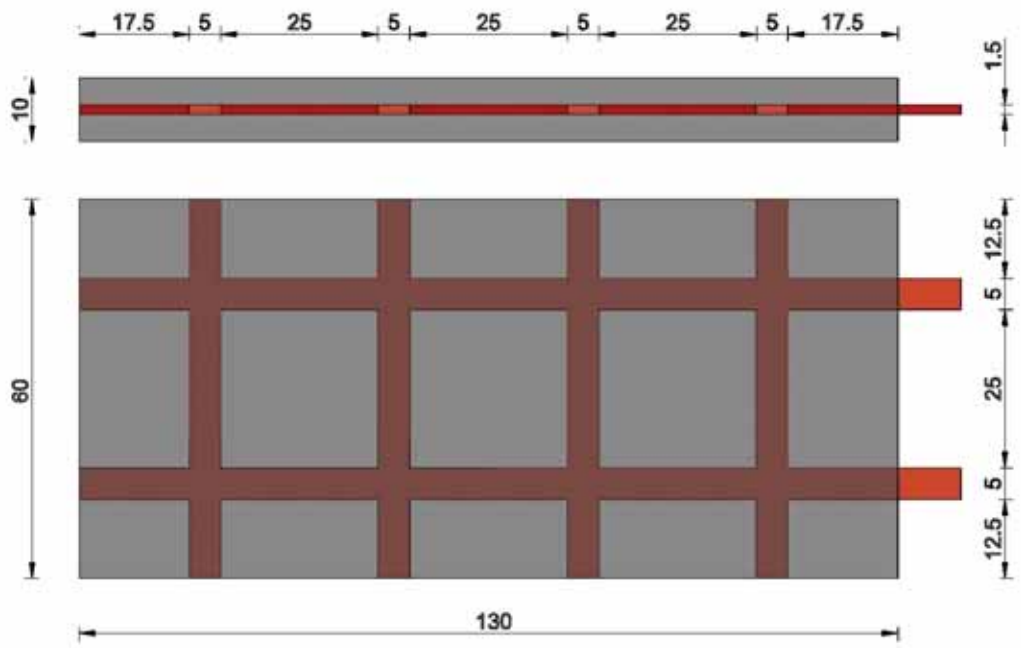

Figure 17. Geometric properties of the specimen (dimensions in mm).

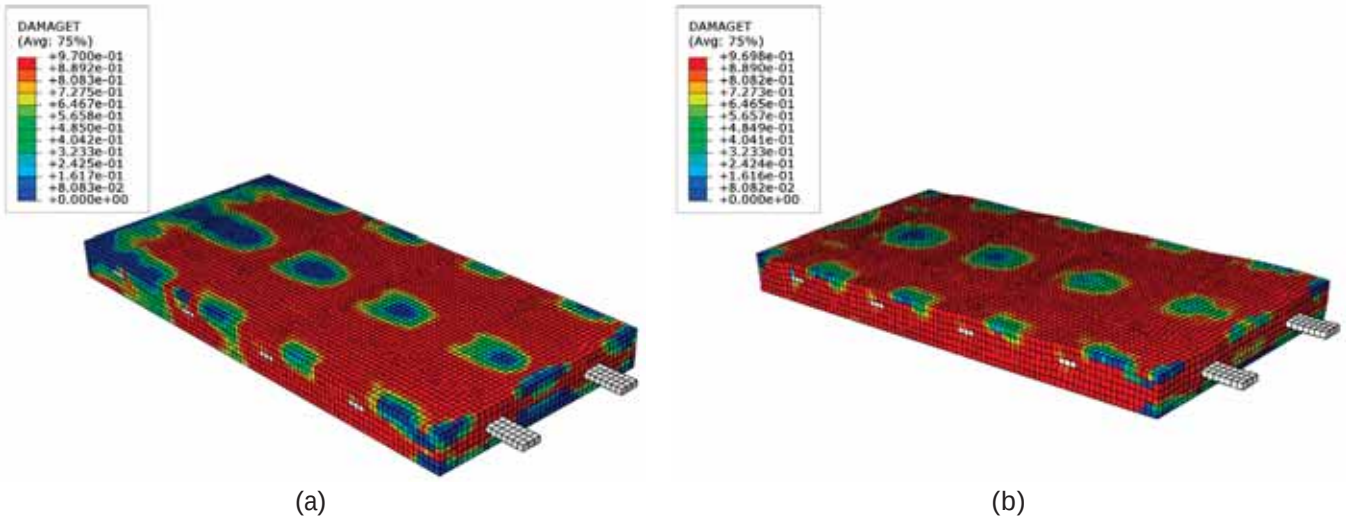

Figure 18. Matrix tensile damage contour for a polynomial (**a**) and exponential (**b**) approximation.

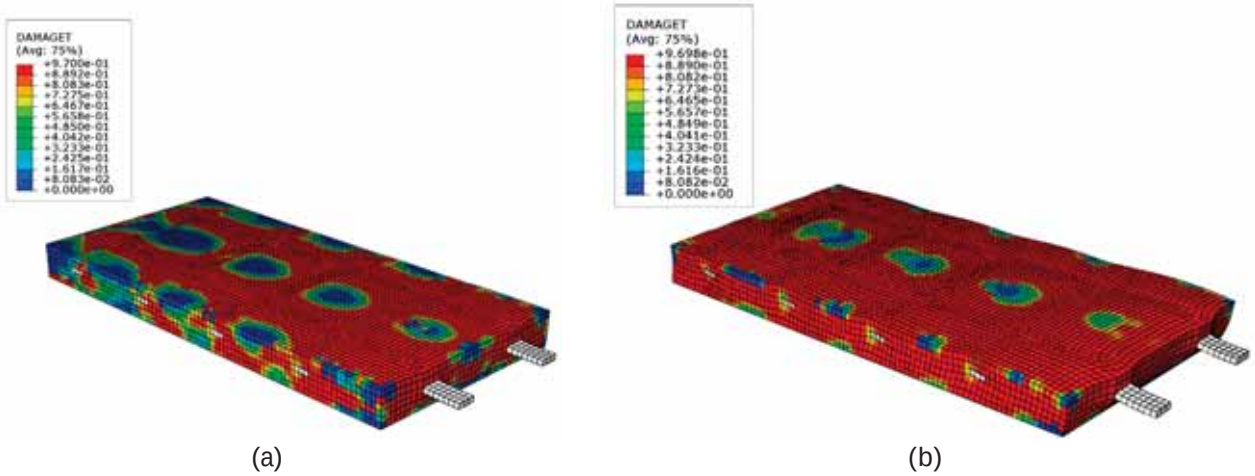

Figure 19. Matrix tensile damage contour for a polynomial (**a**) and exponential (**b**) approximation.

The diagrams corresponding to the results of Figures 18 and 19 are shown in Figure 20, which refers to the load–slip response of the CRM specimen for both types of reinforcements and mechanical laws, with a clear overall increase in strength and ductility compared to the previous simplified specimen. Furthermore, in this case, the softening branch is more pronounced for wet fibers compared to the case of dry carbon fibers, while assuming a higher value of peak load for lower values of slip, together with an increased initial stiffness.

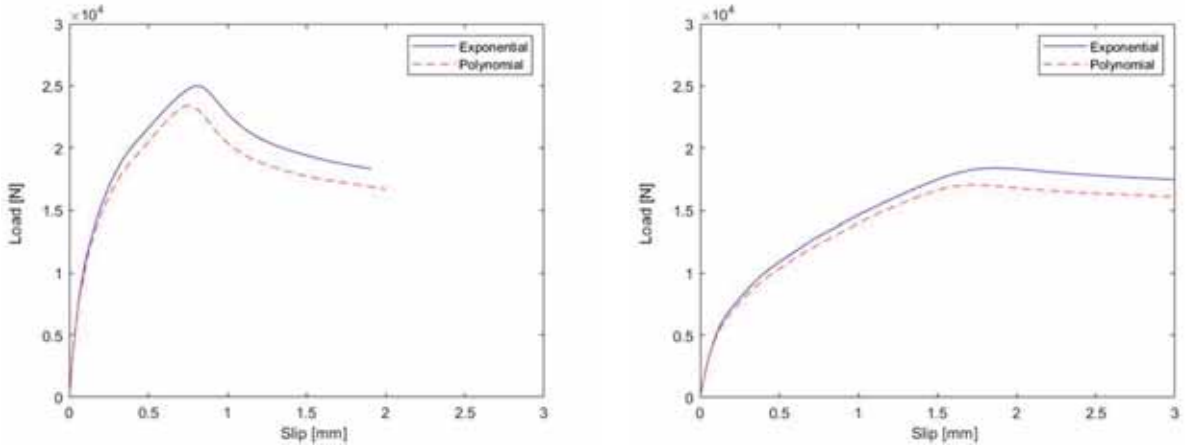

Figure 20. Comparison of the results for wet (**a**) and dry (**b**) carbon fibers.

The same specimen was then modeled by applying a cohesive fiber–matrix interface, with the same properties used for the reduced sample, whose contour plots for the traction damage of the mortar are represented in Figure 21, with a meaningful variation in terms of intensity and expansion compared to Figure 19. This is now more pronounced in the transversal direction rather than the longitudinal direction, with an early collapse compared to the perfectly bonded example, as plotted in Figure 22 for the CRM specimen with wet fibers. In the present case, indeed, the sample undergoes a sudden break soon after the decohesion of the fibers from the mortar, without highlighting any softening branch or a recovery stage in terms of resistance as shown in the previous example.

Finally, a test with periodic type boundary conditions has been analyzed to evaluate the overall response of a CRM reinforcement associated with an actual application of larger dimensions. In particular, displacements U1 and rotations UR1 and UR3 are null in the lateral faces of the specimen, while keeping fixed the contact interface with the substrate. This specimen is characterized by a single longitudinal fiber and four transverse fibers, characterized by the geometric dimensions shown in Figure 23.

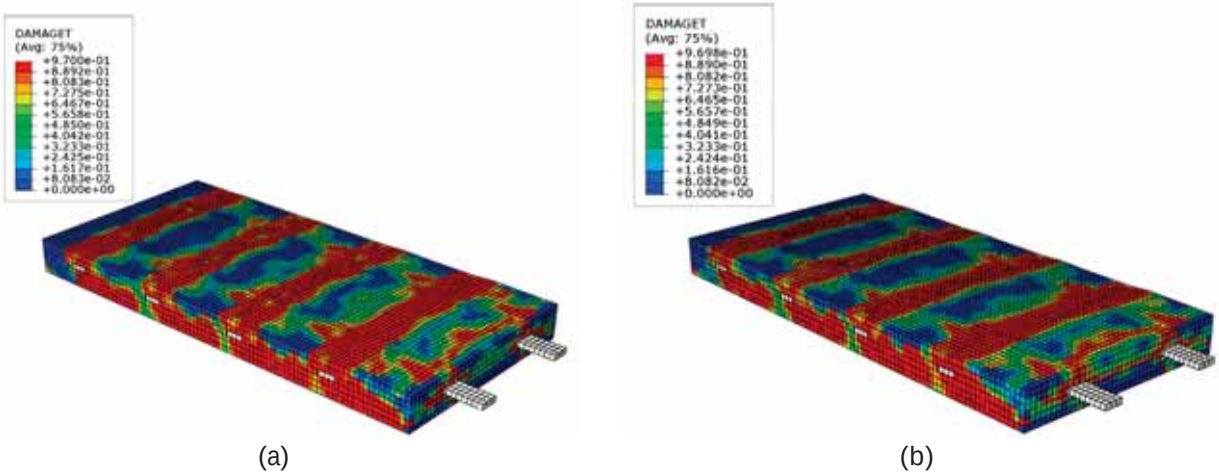

Figure 21. Matrix tensile damage contour for a polynomial (**a**) and exponential (**b**) approximation.

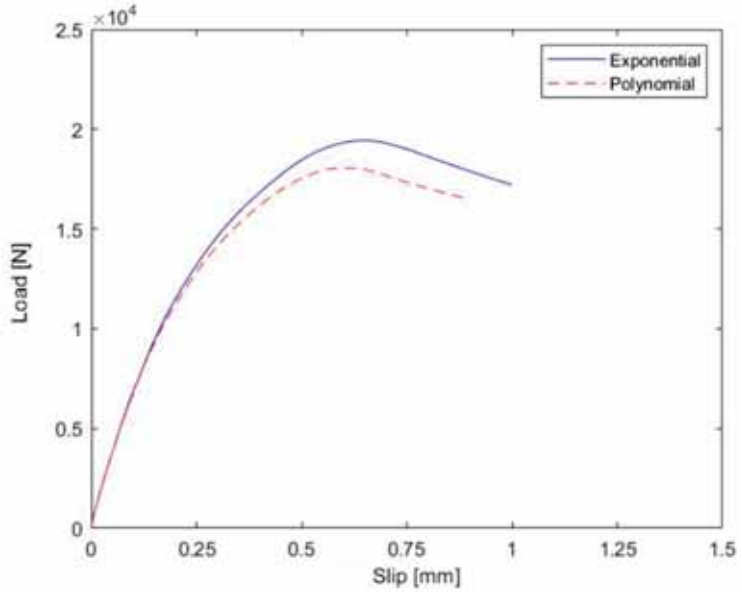

Figure 22. Load vs. slip response of the specimen modeled with a cohesive matrix–fiber interface.

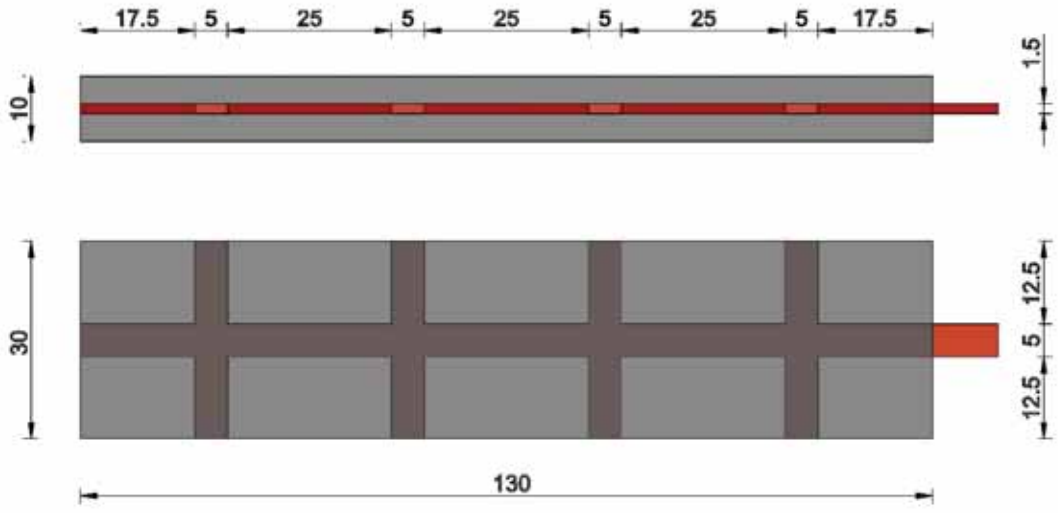

Figure 23. Geometric properties of the specimen (dimensions in mm).

Once again, the tie constraint is enforced at the fiber–matrix interface for the study of mortar damage under the twofold assumption of fiber reinforcement. The contour plots of damage related to this example are shown in Figures 24 and 25 for fibers with a higher and lower stiffness, respectively, whereas the overall time–history response is plotted in Figure 26a,b for both types of fiber properties.

The sample with periodic constraints shows an overall trend similar to those previously discussed. Differently from the specimen with two longitudinal fibers, the peak load value in this case is four times lower, and the ultimate displacement is reduced quantitatively by 67%. Such results cannot be fully considered for real applications, but can estimate the degree of reinforcement given by the transverse fibers, together with the associated different crisis modes, as suitable to tailor the reinforcement design in actual cases.

To consider the mortar–substrate interfacial crisis mode, the specimen has been modeled with reduced geometric properties and cohesive properties at the interfacial level with the substrate for a displacement control test; the details are represented in Figure 27. More specifically, the mortar–substrate cohesive interface is characterized by the maximum nominal stresses in the three directions $f_1 = 5$ MPa, $f_2 = f_3 = 2.5$ MPa, ultimate displacement $w = 0.01$ mm, and stiffness values $K_{nn} = 13000$ MPa and $K_{ss} = K_{tt} = 5500$ MPa in the

normal and tangential directions, respectively. In addition, the interpenetration condition is prevented by setting a 'hard contact' algorithm in the normal direction, as implemented in the numerical code.

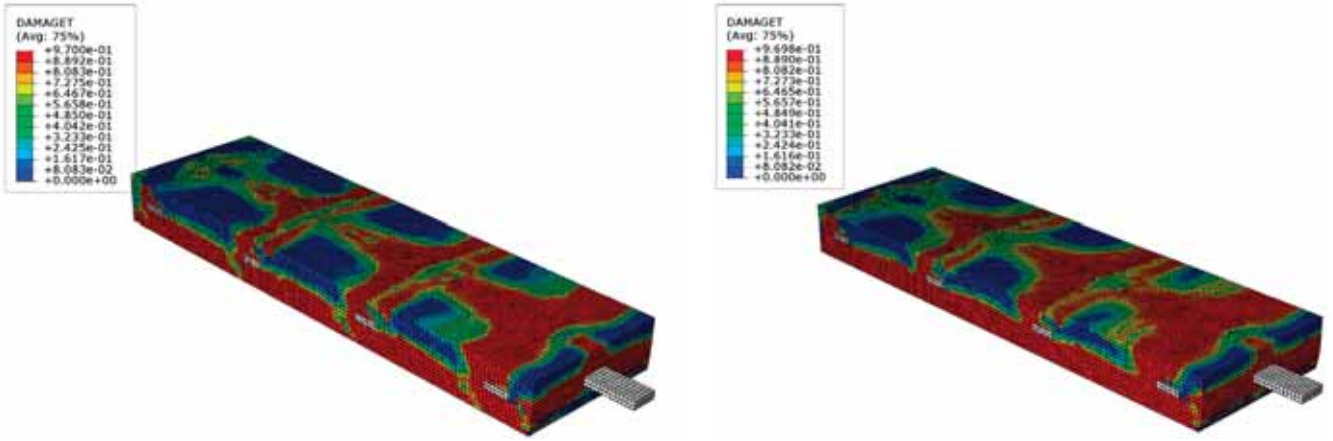

Figure 24. Matrix tensile damage contour for a polynomial (**a**) and exponential (**b**) approximation.

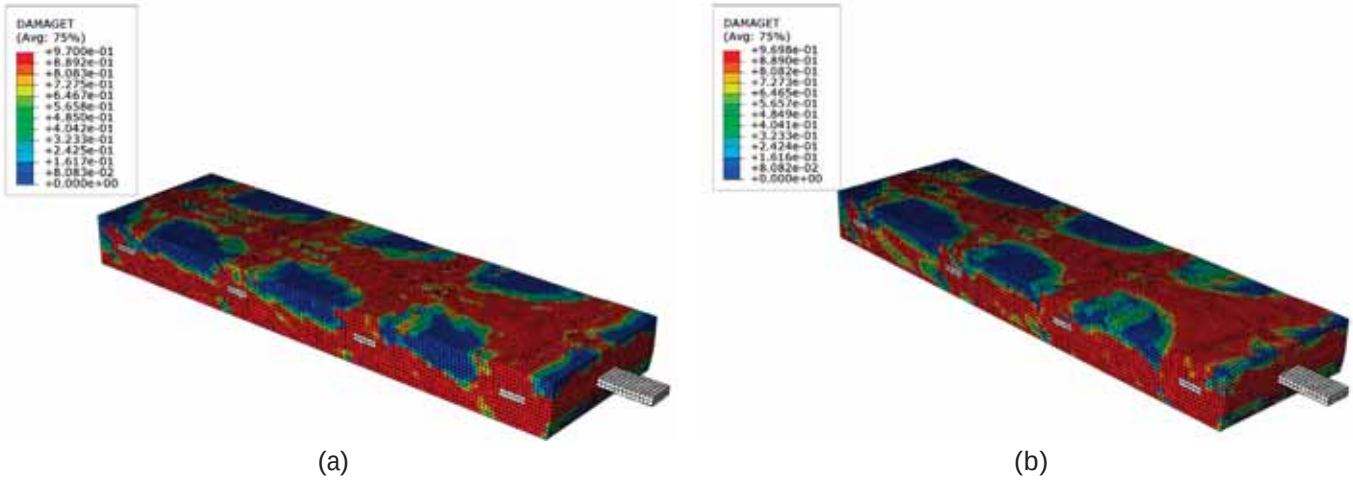

Figure 25. Matrix tensile damage contour for a polynomial (**a**) and exponential (**b**) approximation.

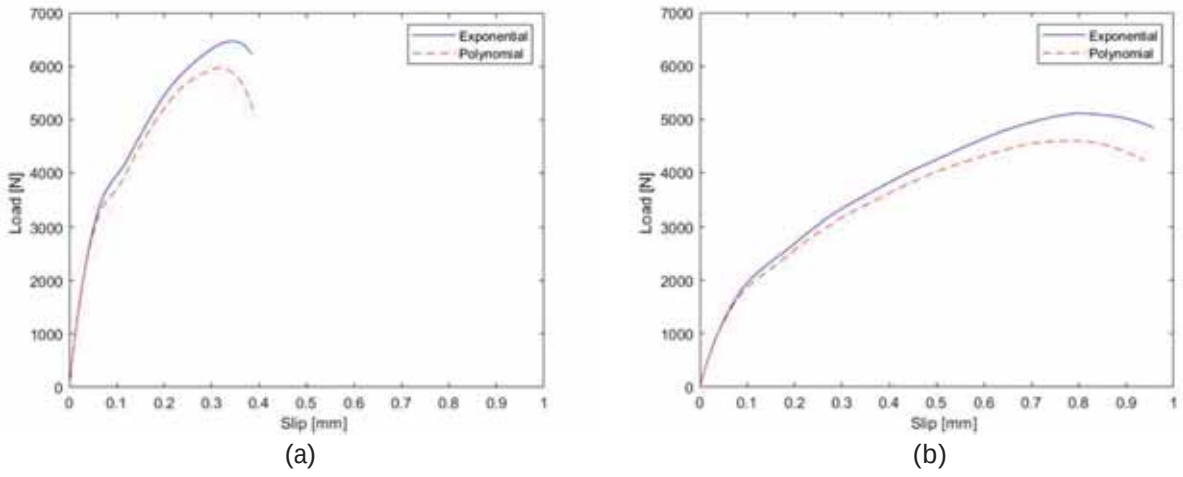

Figure 26. Comparison of the results for wet (**a**) and dry (**b**) carbon fibers.

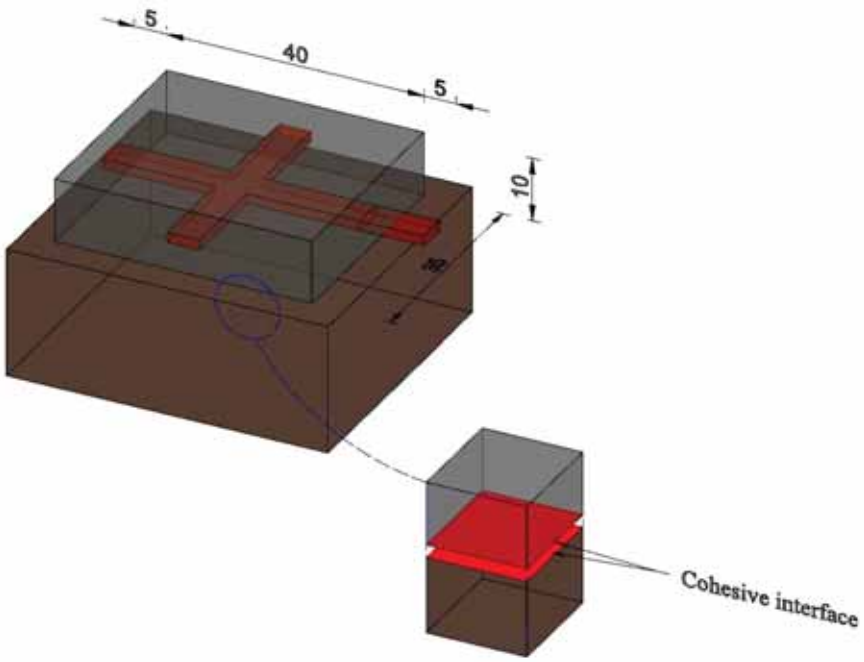

Figure 27. Detail of the matrix–substrate cohesive interfaces.

Figure 28 shows the delamination evolution of the reinforcement phase from the substrate at four different time steps. In particular, the cohesive interface is here represented in 2D, along with the shear stress contour plot in the loading direction. The specimen is loaded on the right side on these plots such that the delamination spreads from the right to the left side.

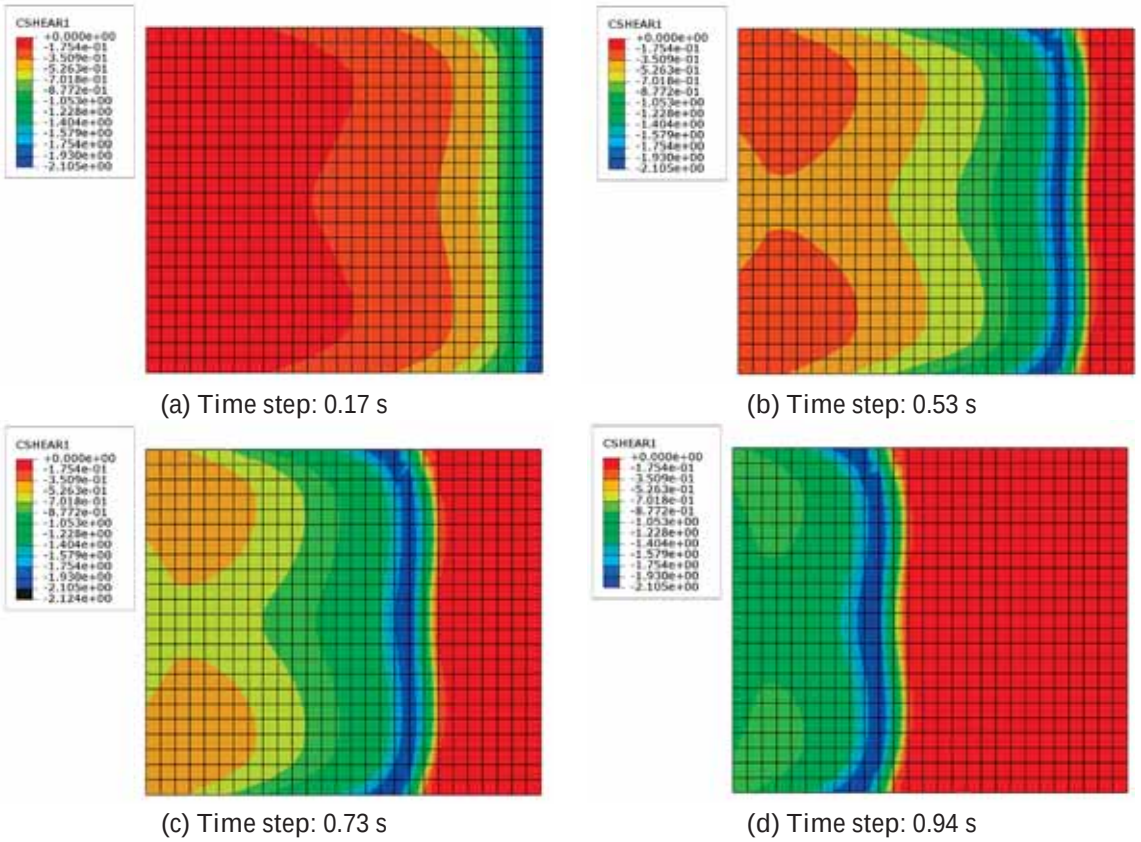

Figure 28. Contour plot evolution of the shear stress in the direction of the applied load—detail of the cohesive interface for the reduced specimen.

Such local evolution of damage corresponds to the global time–history response in Figure 29, with a clear fragile response of the specimen with wet reinforcements, in total absence of a softening branch.

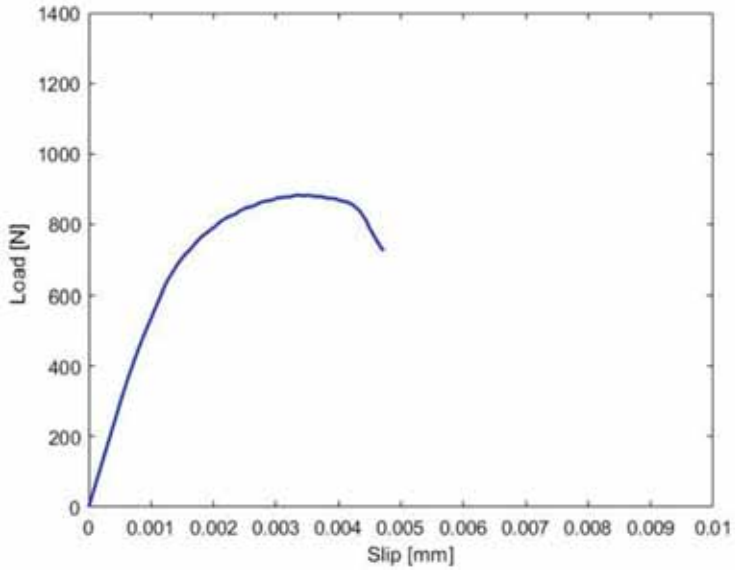

Figure 29. Global response of the specimen with a cohesive matrix–substrate interface.

As a last example, we repeated the test to evaluate the influence of a different number of fibers as reinforcement, using two longitudinal fibers and four transverse ones. The evolution of the shear stress contour plot in the loading direction is shown in Figure 30 at four different time steps, with a clear different localization of the maximum values of the stress state moving from the right to the left side.

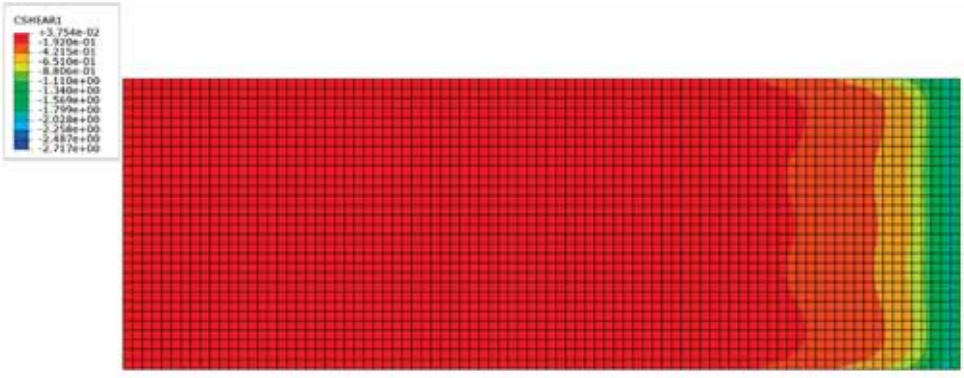

(a) Time step: 6.36×10^{-3} s

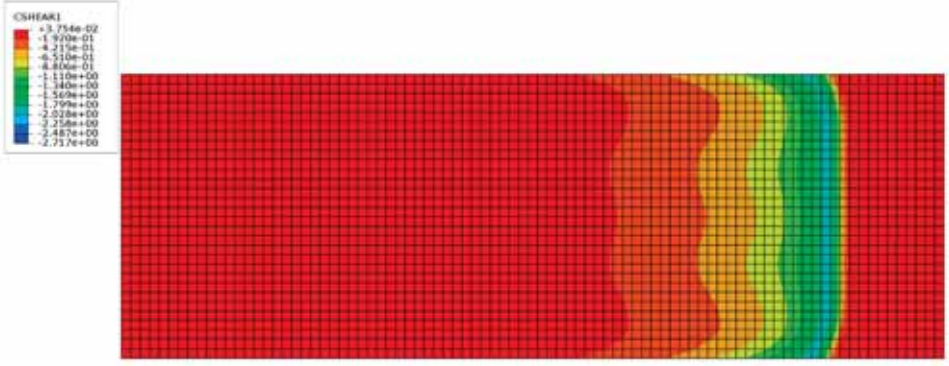

(b) Time step: 2.15×10^{-2} s

Figure 30. *Cont.*

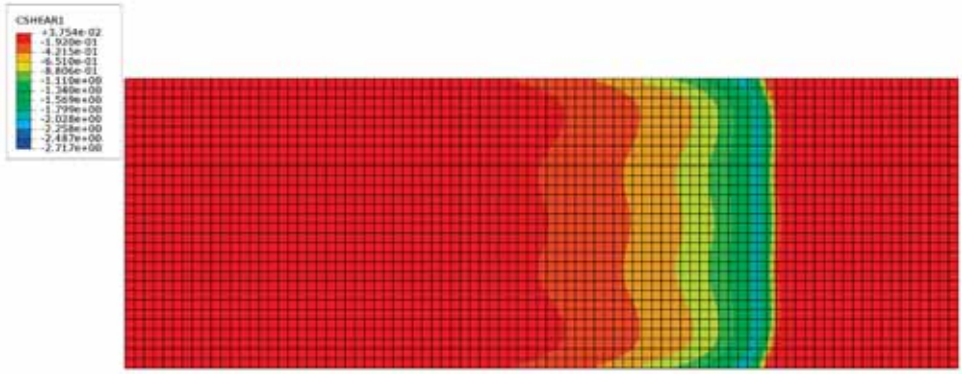

(c) Time step: 2.57×10^{-2} s

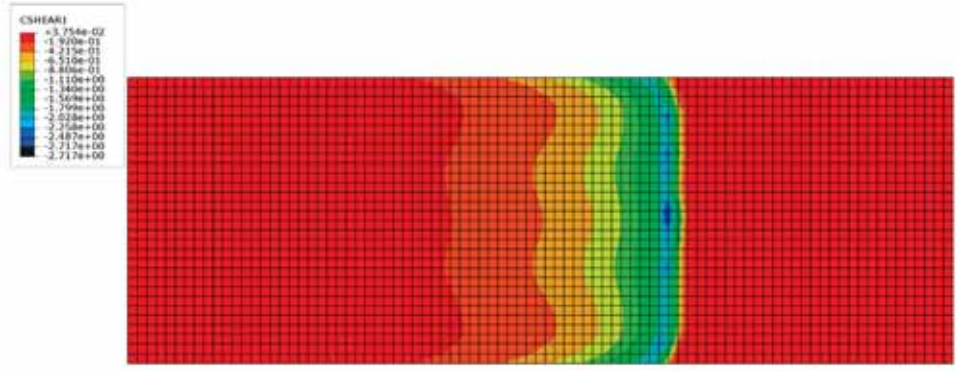

(d) Time step: 4.03×10^{-2} s

Figure 30. Contour plot evolution of the shear stresses in the direction of the applied load—detail of the cohesive interface.

In such a case, the global load–slip response features a more ductile behavior, as visible in Figure 31. In this case, the curve undergoes a plastic softening after the peak load, whose value is higher in this case than the one obtained for a delaminating reduced specimen. This post-peak behavior stems from the higher redistribution of the local stress state due to the presence of an increased number of fibers in the transverse direction, thus justifying the sensitivity of the mechanical response to the reinforcing distribution.

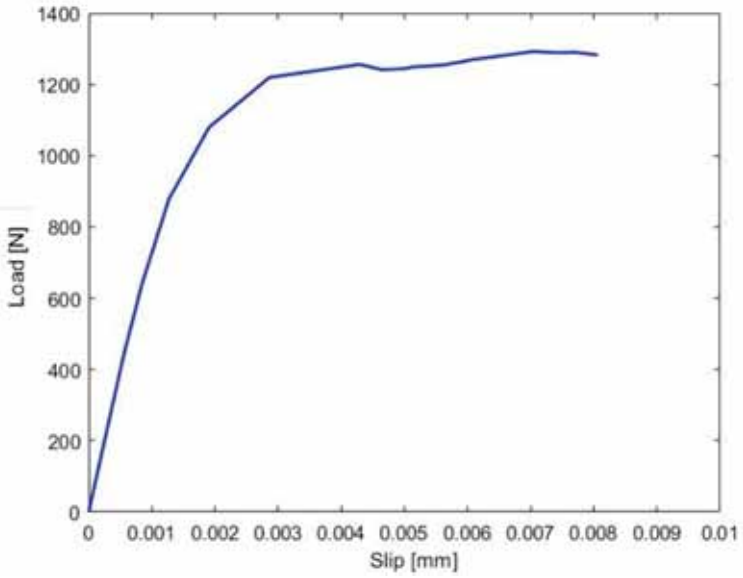

Figure 31. Global response of the specimen with a cohesive matrix–substrate interface.

5. Conclusions

The present work has studied numerically a CRM reinforcement system for existing structures consisting of an inorganic mortar and a pre-impregnated fibers net, as a valid alternative to traditional reinforcements, due to its non-intrusiveness, reversibility, and lightness of the thin mortar thickness. This study was inspired by Ref. [35], where a CRM reinforcement system is here modeled, instead of a dry and transversely isotropic fiber FRCM sample, whose tensile and compressive mechanical behavior has been approximated analytically by means of two different laws, i.e., an exponential and polynomial law. Such analytical definitions of the mechanical properties both in tension and compression have then been implemented in the numerical finite element code for a proper description of the nonlinear fracturing processes for the selected problem, involving the mortar, the substrate, and the interfacial substrate–matrix system. To this end, a concrete damage plasticity model and cohesive zone modeling are here employed as valid tools to interpret similar fracturing problems, where two types of net have been assumed here: one dry and transversally isotropic, in line with Ref. [35]; and another one with isotropic properties and pre-impregnated, typical of CRM systems. A systematic analysis has considered three different sizes of single-lap shear specimens, involving also periodic boundary conditions, whose numerical approaches and general conclusions in terms of damage distribution and time–history response could serve as valid tools for practical strengthening design. Based on the numerical campaign, for each selected case, a polynomial approximation of the matrix properties provides always more conservative results compared to an exponential approximation in the nonlinear part of the load–slip curves, due to the different intrinsic nature of both mathematical functions. A perfectly bonded CRM specimen rather than a cohesive contact modeling of interfaces can be responsible for different damage and stress distributions within specimens, thus varying not only their initial stiffness but also their maximum strength and ductility/fragility before the complete fracture.

In general, the presence of a cohesive fiber–matrix interface seems to yield an early collapse compared to the perfectly bonded example, soon after the decohesion of the fibers from the mortar, without highlighting any softening branch or recovery stage in terms of resistance. The global load–slip response assumes a more ductile behavior for specimens with an increased number of fibers, both in the longitudinal and transverse directions under periodic boundary conditions, due to an increased redistribution of the local stress state within the specimen. A further expansion of the work will consider an experimental investigation on the topic and the possible application of more advanced computational tools, such as the extended finite element method, to predict any possible multiple crack propagation and directions.

Author Contributions: Conceptualization, R.D., M.T. and F.T.; Data curation, M.R.; Formal analysis, R.D., M.R., M.T. and F.T.; Investigation, R.D., M.R., M.T. and F.T.; Methodology, R.D., M.T. and F.T.; Software, M.R.; Supervision, R.D. and F.T.; Validation, R.D., M.R., M.T. and F.T.; Writing—Original draft, R.D., M.R., M.T. and F.T.; Writing—Review & editing, R.D., M.T. and F.T. All authors have read and agreed to the published version of the manuscript.

Funding: This work is supported by ICSC—Centro Nazionale di Ricerca in High Performance Computing, Big Data and Quantum Computing, funded by European Union—Next Generation EU.

Conflicts of Interest: The authors declare no conflict of interest.

References

1. Marcari, G.; Manfredi, G.; Prota, A.; Pecce, M. In-plane shear performance of masonry panels strengthened with FRP. *Compos. Part B Eng.* **2007**, *38*, 887–901. [CrossRef]
2. Sassoni, E.; Sarti, V.; Bellini, A.; Mazzotti, C.; Franzoni, E. The role of mortar joints in FRP debonding from masonry. *Compos. Part B Eng.* **2017**, *135*, 166–174. [CrossRef]
3. Guerreiro, J.; Proença, J.; Ferreira, J.G.; Gago, A. Experimental characterization of in-plane behaviour of old masonry walls strengthened through the addition of CFRP reinforced render. *Compos. Part B Eng.* **2018**, *148*, 14–26. [CrossRef]

4. Jafari, A.; Oskouei, A.V.; Bazli, M.; Ghahri, R. Effect of the FRP sheet's arrays and NSM FRP bars on in-plane behavior of URM walls. *J. Build. Eng.* **2018**, *20*, 679–695. [CrossRef]
5. Del Vecchio, C.; Di Ludovico, M.; Balsamo, A.; Prota, A.; Manfredi, G.; Dolce, M. Experimental Investigation of Exterior RC Beam-Column Joints Retrofitted with FRP Systems. *J. Compos. Constr.* **2014**, *18*, 04014002. [CrossRef]
6. Del Zoppo, M.; Di Ludovico, M.; Balsamo, A.; Prota, A.; Manfredi, G. FRP for seismic strengthening of shear controlled RC columns: Experience from earthquakes and experimental analysis. *Compos. Part B Eng.* **2017**, *129*, 47–57. [CrossRef]
7. Del Zoppo, M.; Di Ludovico, M.; Balsamo, A.; Prota, A. Comparative analysis of existing RC columns jacketed with CFRP or FRCC. *Polymers* **2018**, *10*, 361. [CrossRef]
8. Aiello, M.A.; Leone, M. Interface analysis between FRP EBR system and concrete. *Compos. Part B Eng.* **2008**, *39*, 618–626. [CrossRef]
9. Ferrari, L. First-aid and provisional devices in historical structures with collapse risk after seismic shock. *Key Eng. Mater.* **2019**, *817*, 301–308. [CrossRef]
10. Wu, Z.; Yin, J. Fracturing behaviors of FRP-strengthened concrete structures. *Eng. Fract. Mech.* **2003**, *70*, 1339–1355. [CrossRef]
11. Bocciarelli, M.; Pisani, M.A. Survey on the interface behaviour in reinforced concrete beams strengthened with externally bonded FRP reinforcement. *Compos. Part B Eng.* **2017**, *118*, 169–176. [CrossRef]
12. Chen, J.F.; Teng, J.G. Anchorage Strength Models for Frp and Steel Plates bonded to concrete. *J. Struct. Eng.* **2001**, *127*, 784–791.
13. Dai, J.; Ueda, T.; Sato, Y. Development of the Nonlinear Bond Stress–Slip Model of Fiber Reinforced Plastics Sheet–Concrete Interfaces with a Simple Method. *J. Compos. Constr.* **2005**, *9*, 52–62. [CrossRef]
14. Lu, X.Z.; Teng, J.G.; Ye, L.P.; Jiang, J.J. Bond–slip models for FRP sheets/plates bonded to concrete. *Eng. Struct.* **2005**, *27*, 920–937. [CrossRef]
15. Wu, Z.; Islam, S.; Said, H. A Three-parameter bond strength model for FRP—Concrete interface. *J. Reinf. Plast. Compos.* **2009**, *28*, 2309–2323. [CrossRef]
16. Hosseini, A.; Mostofinejad, D. Effective bond length of FRP-to-concrete adhesively-bonded joints: Experimental evaluation of existing models. *Int. J. Adhes. Adhes.* **2014**, *48*, 150–158. [CrossRef]
17. Mofrad, M.H.; Mostofinejad, D.; Hosseini, A. A generic non-linear bond-slip model for CFRP composites bonded to concrete substrate using EBR and EBROG techniques. *Compos. Struct.* **2019**, *220*, 31–44. [CrossRef]
18. Shi, J.-W.; Cao, W.-H.; Wu, Z.-S. Effect of adhesive properties on the bond behaviour of externally bonded FRP-to-concrete joints. *Compos. Part B Eng.* **2019**, *177*, 107365. [CrossRef]
19. Wu, Y.-F.; He, L. Width effect of interfacial bond characteristics. *Constr. Build. Mater.* **2019**, *220*, 712–726. [CrossRef]
20. Gattesco, N.; Boem, I.; Dudine, A. Diagonal compression tests on masonry walls strengthened with a GFRP mesh reinforced mortar coating. *Bull. Earthq. Eng.* **2015**, *13*, 1703–1726. [CrossRef]
21. D'antino, T.; Carozzi, F.G.; Poggi, C. Diagonal shear behavior of historic walls strengthened with composite reinforced mortar (CRM). *Mater. Struct.* **2019**, *52*, 114. [CrossRef]
22. Del Zoppo, M.; Di Ludovico, M.; Balsamo, A.; Prota, A. In-plane shear capacity of tuff masonry walls with traditional and innovative Composite Reinforced Mortars (CRM). *Constr. Build. Mater.* **2019**, *210*, 289–300. [CrossRef]
23. Tilocca, A.R.; Incerti, A.; Bellini, A.; Savoia, M. Influence of matrix properties on frcm-crm strengthening systems. *Key Eng. Mater.* **2019**, *817*, 478–485. [CrossRef]
24. D'antino, T.; Calabrese, A.S.; Poggi, C.; Colombi, P.; Fava, G.; Bocciarelli, M. Strengthening of different types of slabs with composite-reinforced mortars (CRM). In *Buildings for Education*; Springer: Cham, Switzerland, 2020; pp. 293–303. [CrossRef]
25. D'antino, T.; Calabrese, A.S.; Poggi, C. Experimental procedures for the mechanical characterization of composite reinforced mortar (CRM) systems for retrofitting of masonry structures. *Mater. Struct.* **2020**, *53*, 94. [CrossRef]
26. Gattesco, N.; Rizzi, E.; Bez, A.; Dudine, A. ScienceDirect Study on the effectiveness of a CRM system: In-plane and out-of-plane cyclic tests on masonry piers. *Procedia Struct. Integr.* **2022**, *44*, 2230–2237. [CrossRef]
27. Longo, F.; Cascardi, A.; Lassandro, P.; Aiello, M.A. A Novel Composite Reinforced Mortar for the Structural and Energy Retrofitting of Masonry Panels. *Key Eng. Mater.* **2022**, *916*, 377–384. [CrossRef]
28. Tamborrino, O.; Perrone, D.; Leone, M. Numerical modelling of shear bond tests on externally strengthened masonry specimens. In Proceedings of the COMPDYN Proceeding, Athens, Greece, 28–30 June 2021; pp. 4729–4741. [CrossRef]
29. Tamborrino, O.; Perrone, D.; Leone, M.; Aiello, M.A. Experimental Study on the Fiber-Matrix Interface Behavior of FRCM/CRM Reinforcement Systems. *Key Eng. Mater.* **2022**, *916*, 409–416. [CrossRef]
30. Kouris, L.A.S.; Triantafillou, T.C. State-of-the-art on strengthening of masonry structures with textile reinforced mortar (TRM). *Constr. Build. Mater.* **2018**, *188*, 1221–1233. [CrossRef]
31. Consiglio Superiore dei Lavori Pubblici. *Linea Guida per la Identificazione, la Qualificazione ed il Controllo di Accettazione dei Sistemi a Rete Preformata in Materiali Compositi Fibrorinforzati a Matrice Polimerica da Utilizzarsi per il Consolidamento Strutturale di Costruzioni Esistenti con la Tecnica Dell'intonaco Armato CRM (Composite Reinforced Mortar)*; Consiglio Superiore dei Lavori Pubblici: Roma, Italy, 2019.
32. Salomoni, V.; Mazzucco, G.; Pellegrino, C.; Majorana, C. Three-dimensional modelling of bond behaviour between concrete and FRP reinforcement. *Eng. Comput.* **2011**, *28*, 5–29. [CrossRef]

33. Motamedi, D.; Milani, A.S. 3D Nonlinear XFEM Simulation of Delamination in Unidirectional Composite Laminates: A Sensitivity Analysis of Modeling Parameters. *Open J. Compos. Mater.* **2013**, *3*, 113–126. [CrossRef]
34. Yu, H.; Bai, Y.-L.; Dai, J.-G.; Gao, W.-Y. Finite element modeling for debonding of frp-to-concrete interfaces subjected to mixed-mode loading. *Polymers* **2017**, *9*, 438. [CrossRef]
35. Mazzucco, G.; D'Antino, T.; Pellegrino, C.; Salomoni, V. Three-dimensional finite element modeling of inorganic-matrix composite materials using a mesoscale approach. *Compos. Part B Eng.* **2017**, *143*, 75–85. [CrossRef]
36. Grande, E.; Imbimbo, M.; Marfia, S.; Sacco, E. Numerical simulation of the de-bonding phenomenon of FRCM strengthening systems. *Procedia Struct. Integr.* **2018**, *9*, 257–264. [CrossRef]
37. Ombres, L.; Iorfida, A.; Verre, S. FRCM/SRG—Masonry joints: Experimental investigation and numerical modelling. *Key Eng. Mater.* **2019**, *817*, 3–8. [CrossRef]
38. Consiglio Superiore dei Lavori Pubblici. *Linea Guida per la Identificazione, la Qualificazione ed il Controllo di Accettazione di Compositi Fibrorinforzati a Matrice Inorganica (FRCM) da Utilizzarsi per il Consolidamento Strutturale di Costruzioni Esistenti*; Consiglio Superiore dei Lavori Pubblici: Roma, Italy, 2018.
39. Dimitri, R.; Trullo, M.; De Lorenzis, L.; Zavarise, G. Coupled cohesive zone models for mixed-mode fracture: A comparative study. *Eng. Fract. Mech.* **2015**, *148*, 145–179. [CrossRef]
40. Barenblatt, G. The formation of equilibrium cracks during brittle fracture. General ideas and hypotheses. Axially-symmetric cracks. *J. Appl. Math. Mech.* **1959**, *23*, 622–636. [CrossRef]
41. Barenblatt, G.I. The Mathematical Theory of Equilibrium Cracks in Brittle Fracture. *Adv. Appl. Mech.* **1962**, *7*, 55–129.
42. Dugdale, D.S. Yielding of steel sheets containing slits. *J. Mech. Phys. Solids* **1960**, *8*, 100–104. [CrossRef]
43. Hillerborg, A.; Modéer, M.; Petersson, P.-E. Analysis of crack formation and crack growth in concrete by means of fracture mechanics and finite elements. *Cem. Concr. Res.* **1976**, *6*, 773–781. [CrossRef]
44. Tvergaard, V. Effect of fibre debonding in a whisker-reinforced metal. *Mater. Sci. Eng. A* **1990**, *125*, 203–213. [CrossRef]
45. Camacho, G.; Ortiz, M. Computational modelling of impact damage in brittle materials. *Int. J. Solids Struct.* **1996**, *33*, 2899–2938. [CrossRef]
46. Espinosa, H.; Dwivedi, S.; Lu, H.-C. Modeling impact induced delamination of woven fiber reinforced composites with contact/cohesive laws. *Comput. Methods Appl. Mech. Eng.* **2000**, *183*, 259–290. [CrossRef]
47. Foulk, J.; Allen, D.; Helms, K. Formulation of a three-dimensional cohesive zone model for application to a finite element algorithm. *Comput. Methods Appl. Mech. Eng.* **2000**, *183*, 51–66. [CrossRef]
48. Rahulkumar, P.; Jagota, A.; Bennison, S.; Saigal, S. Cohesive element modeling of viscoelastic fracture: Application to peel testing of polymers. *Int. J. Solids Struct.* **2000**, *37*, 1873–1897. [CrossRef]
49. Siegmund, T.; Brocks, W. A numerical study on the correlation between the work of separation and the dissipation rate in ductile fracture. *Eng. Fract. Mech.* **2000**, *67*, 139–154. [CrossRef]
50. Li, H.; Chandra, N. Analysis of crack growth and crack-tip plasticity in ductile materials using cohesive zone models. *Int. J. Plast.* **2003**, *19*, 849–882. [CrossRef]
51. Freed, Y.; Banks-Sills, L. A new cohesive zone model for mixed mode interface fracture in bimaterials. *Eng. Fract. Mech.* **2008**, *75*, 4583–4593. [CrossRef]
52. Chen, X.; Deng, X.; Sutton, M.A.; Zavattieri, P. An inverse analysis of cohesive zone model parameter values for ductile crack growth simulations. *Int. J. Mech. Sci.* **2014**, *79*, 206–215. [CrossRef]
53. Dimitri, R.; De Lorenzis, L.; Wriggers, P.; Zavarise, G. NURBS- and T-spline-based isogeometric cohesive zone modeling of interface debonding. *Comput. Mech.* **2014**, *54*, 369–388. [CrossRef]
54. Jiang, L.; Nath, C.; Samuel, J.; Kapoor, S.G. Estimating the Cohesive Zone Model Parameters of Carbon Nanotube–Polymer Interface for Machining Simulations. *J. Manuf. Sci. Eng.* **2014**, *136*, 031004. [CrossRef]
55. Yang, Q.; Schesser, D.; Niess, M.; Wright, P.; Mavrogordato, M.; Sinclair, I.; Spearing, S.; Cox, B. On crack initiation in notched, cross-plied polymer matrix composites. *J. Mech. Phys. Solids* **2015**, *78*, 314–332. [CrossRef]
56. Needleman, A. An analysis of tensile decohesion along an interface. *J. Mech. Phys. Solids* **1990**, *38*, 289–324. [CrossRef]
57. Xu, X.-P.; Needleman, A. Void nucleation by inclusion debonding in a crystal matrix. *Model. Simul. Mater. Sci. Eng.* **1993**, *1*, 111–132. [CrossRef]
58. Xu, X.-P.; Needleman, A. Numerical simulations of fast crack growth in brittle solids. *J. Mech. Phys. Solids* **1994**, *42*, 1397–1434. [CrossRef]
59. Yang, B.; Mall, S.; Ravi-Chandar, K. A cohesive zone model for fatigue crack growth in quasibrittle materials. *Int. J. Solids Struct.* **2001**, *38*, 3927–3944. [CrossRef]
60. Erarslan, N.; Williams, D.J. Mixed-Mode Fracturing of Rocks Under Static and Cyclic Loading. *Rock Mech. Rock Eng.* **2013**, *46*, 1035–1052. [CrossRef]
61. Li, H.; Yuan, H.; Li, X. Assessment of low cycle fatigue crack growth under mixed-mode loading conditions by using a cohesive zone model. *Int. J. Fatigue* **2015**, *75*, 39–50. [CrossRef]
62. Camanho, P.P.; Davila, C.G.; de Moura, M.F. Numerical Simulation of Mixed-Mode Progressive Delamination in Composite Materials. *J. Compos. Mater.* **2003**, *37*, 1415–1438. [CrossRef]

63. Pantano, A.; Averill, R.C. A mesh-independent interface technology for simulation of mixed-mode delamination growth. *Int. J. Solids Struct.* **2004**, *41*, 3809–3831. [CrossRef]
64. Bosch, M.v.D.; Schreurs, P.; Geers, M. An improved description of the exponential Xu and Needleman cohesive zone law for mixed-mode decohesion. *Eng. Fract. Mech.* **2006**, *73*, 1220–1234. [CrossRef]
65. Dávila, C.G.; Rose, C.A.; Camanho, P.P. A procedure for superposing linear cohesive laws to represent multiple damage mechanisms in the fracture of composites. *Int. J. Fract.* **2009**, *158*, 211–223. [CrossRef]
66. de Moura, M.; Gonçalves, J. Cohesive zone model for high-cycle fatigue of composite bonded joints under mixed-mode I+II loading. *Eng. Fract. Mech.* **2015**, *140*, 31–42. [CrossRef]
67. Lubliner, J.; Oliver, J.; Oller, S.; Oñate, E. A plastic-damage model for concrete. *Int. J. Solids Struct.* **1989**, *25*, 299–326. [CrossRef]
68. Carol, I.; Rizzi, E.; Willam, K. On the formulation of anisotropic elastic degradation. I. Theory based on a pseudo-logarithmic damage tensor rate. *Int. J. Solids Struct.* **2001**, *38*, 491–518. [CrossRef]
69. de Moura, M.F.S.F. Application of Cohesive Zone Modeling to Composite Bonded Repairs. *J. Adhes.* **2015**, *91*, 71–94. [CrossRef]
70. Dimitri, R.; Tornabene, F.; Zavarise, G. Analytical and numerical modeling of the mixed-mode delamination process for composite moment-loaded double cantilever beams. *Compos. Struct.* **2018**, *187*, 535–553. [CrossRef]
71. Dimitri, R.; Tornabene, F. Numerical Study of the Mixed-Mode Delamination of Composite Specimens. *J. Compos. Sci.* **2018**, *2*, 30. [CrossRef]
72. Dimitri, R.; Tornabene, F.; Reddy, J.N. Numerical study of the mixed-mode behavior of generally-shaped composite interfaces. *Compos. Struct.* **2020**, *237*, 111935. [CrossRef]
73. Dimitri, R.; Rinaldi, M.; Tornabene, F.; Micelli, F. Numerical study of the FRP-concrete bond behavior under thermal variations. *Curved Layered Struct.* **2023**, *10*, 20220193. [CrossRef]
74. Ahmed, B.; Voyiadjis, G.Z.; Park, T. Damaged plasticity model for concrete using scalar damage variables with a novel stress decomposition. *Int. J. Solids Struct.* **2020**, *191–192*, 56–75. [CrossRef]
75. Lee, J.; Fenves, G.L. Plastic-Damage Model for Cyclic Loading of Concrete Structures. *J. Eng. Mech.* **1998**, *124*, 892–900. [CrossRef]
76. Jason, L.; Huerta, A.; Pijaudier-Cabot, G.; Ghavamian, S. An elastic plastic damage formulation for concrete: Application to elementary tests and comparison with an isotropic damage model. *Comput. Methods Appl. Mech. Eng.* **2006**, *195*, 7077–7092. [CrossRef]
77. Grassl, P.; Nyström, U.; Rempling, R.; Gylltoft, K. A damage-plasticity model for the dynamic failure of concrete. In Proceedings of the 8th International Conference on Structural Dynamics, EURODYN, Leuven, Belgium, 4–6 July 2011; pp. 3287–3294.
78. Lee, J.; Fenves, G.L. A nonlinear concrete damaged plasticity model for simulation reinforced concrete structures using ABAQUS. *J. Eng. Mech.* **1998**, *124*, 892–900. [CrossRef]
79. Krätzig, W.B.; Pölling, R. An elasto-plastic damage model for reinforced concrete with minimum number of material parameters. *Comput. Struct.* **2004**, *82*, 1201–1215. [CrossRef]
80. Hordijk, D.A. Local Approach to Fatigue of Concrete. Ph.D. Thesis, Delft University of Technology, Delft, The Netherlands, 1991.
81. Rice, J.R. A Path Independent Integral and the Approximate Analysis of Strain Concentration by Notches and Cracks. *J. Appl. Mech.* **1968**, *35*, 379–386. [CrossRef]
82. Alfano, G.; Crisfield, M.A. Finite element interface models for the delamination analysis of laminated composites: Mechanical and computational issues. *Int. J. Numer. Methods Eng.* **2001**, *50*, 1701–1736. [CrossRef]
83. Chen, J. Predicting Progressive Delamination of Stiffened Fibre-Composite Panel and Repaired Sandwich Panel by Decohesion Models. *J. Thermoplast. Compos. Mater.* **2002**, *15*, 429–442. [CrossRef]
84. Davila, C.; Camanho, P.; de Moura, M. Mixed-mode decohesion elements for analyses of progressive delamination. In Proceedings of the 19th AIAA Applied Aerodynamics Conference, Anaheim, CA, USA, 11–14 June 2001. [CrossRef]
85. Wells, G.N.; Sluys, L.J. A new method for modelling cohesive cracks using finite elements. *Int. J. Numer. Methods Eng.* **2001**, *50*, 2667–2682. [CrossRef]
86. Valluzzi, M.R.; Oliveira, D.V.; Caratelli, A.; Castori, G.; Corradi, M.; de Felice, G.; Garbin, E.; Garcia, D.; Garmendia, L.; Grande, E.; et al. Round Robin Test for composite-to-brick shear bond characterization. *Mater. Struct.* **2012**, *45*, 1761–1791. [CrossRef]
87. Carozzi, F.G.; Colombi, P.; Poggi, C. Calibration of end-debonding strength model for FRP-reinforced masonry. *Compos. Struct.* **2015**, *120*, 366–377. [CrossRef]
88. De Santis, S.; Ceroni, F.; de Felice, G.; Fagone, M.; Ghiassi, B.; Kwiecień, A.; Lignola, G.P.; Morganti, M.; Santandrea, M.; Valluzzi, M.R.; et al. Round Robin Test on tensile and bond behaviour of Steel Reinforced Grout systems. *Compos. Part B Eng.* **2017**, *127*, 100–120. [CrossRef]
89. Ombres, L.; Mancuso, N.; Mazzuca, S.; Verre, S. Bond between Carbon Fabric-Reinforced Cementitious Matrix and Masonry Substrate. *J. Mater. Civ. Eng.* **2019**, *31*, 04018356. [CrossRef]
90. Carozzi, F.G.; Arboleda, D.; Poggi, C.; Nanni, A. Direct Shear Bond Tests of Fabric-Reinforced Cementitious Matrix Materials. *J. Compos. Constr.* **2020**, *24*, 04019061. [CrossRef]
91. Drdácký, M.; Mašín, D.; Mekonone, M.; Slížková, Z. Compression tests on non-standard historic mortar specimens. In Proceedings of the Historical Mortars Conference HMC08, Lisbon, Portugal, 1 January 2008. Available online: https://web.natur.cuni.cz/uhigug/masin/download/DMMS_HMC08.pdf (accessed on 1 January 2008).

92. Tan, Y.; Gu, Q.; Ning, J.; Liu, X.; Jia, Z.; Huang, D. Uniaxial compression behavior of cement mortar and its damage-constitutive model based on energy theory. *Materials* **2019**, *12*, 1309. [CrossRef]
93. Gao, X.; Zhou, L.; Ren, X.; Li, J. Rate effect on the stress–strain behavior of concrete under uniaxial tensile stress. *Struct. Concr.* **2021**, *22*, E815–E830. [CrossRef]